Boundary measurement tomography of the Bose Hubbard model on general graphs

Abhi Saxena , 1,* Erfan Abbasgholinejad , 1,* Arka Majumdar, 1,2 and Rahul Trivedi , † ¹Department of Electrical & Computer Engineering, University of Washington, Seattle, Washington 98195, USA ²Department of Physics, University of Washington, Seattle, Washington 98195, USA

(Received 16 November 2023; accepted 21 June 2024; published 12 July 2024)

Correlated quantum many-body phenomena in lattice models have been identified as a set of physically interesting problems that cannot be solved classically. Analog quantum simulators, in photonics and microwave superconducting circuits, have emerged as near-term platforms to address these problems. An important ingredient in practical quantum simulation experiments is the tomography of the implemented Hamiltonians—while this can easily be performed if we have individual measurement access to each qubit in the simulator, this could be challenging to implement in many hardware platforms. In this paper, we present a scheme for tomography of quantum simulators which can be described by a Bose-Hubbard Hamiltonian while having measurement access to only some sites on the boundary of the lattice. We present an algorithm that uses the experimentally routine transmission and two-photon correlation functions, measured at the boundary, to extract the Hamiltonian parameters at the standard quantum limit. Furthermore, by building on quantum enhanced spectroscopy protocols that, we show that with the additional ability to switch on and off the on-site repulsion in the simulator, we can sense the Hamiltonian parameters beyond the standard quantum limit.

DOI: 10.1103/PhysRevResearch.6.033058

I. INTRODUCTION

Correlated quantum many-body effects are often hard to simulate on classical computers and have been the subject of considerable recent interest as potential problems to probe with quantum simulators. There has been considerable progress in engineering interacting bosonic modes with on-site nonlinearity in superconducting systems or photonics [1–6], and this has made these some of the most promising analog quantum simulation platforms for studying manybody physics. An important ingredient in the goal of using quantum simulators are protocols that allow accurate tomography of the implemented Hamiltonians [7] with only modest measurement and initial state preparation apparatus. If the experimental system allows measurement and state preparation access to arbitrary sites in the lattice, direct tomography can be performed to characterize the implemented Hamiltonian [8,9]. However, in many experimentally relevant settings [10–12], implementing measurement access to a node in the interior of the lattice is significantly more challenging than the nodes on the outermost boundary that can be accessed for accurate measurements. This experimental requirement raises an important theoretical question: Is it possible to perform tomography of the implemented Hamiltonian with access restricted to only the boundaries of the lattice?

Published by the American Physical Society under the terms of the Creative Commons Attribution 4.0 International license. Further distribution of this work must maintain attribution to the author(s) and the published article's title, journal citation, and DOI.

This question has been considered in previous works, which have proposed tomography algorithms with restricted measurement access to the boundary or a subpart of the lattice. In the setting of one-dimensional chains as well as for more general graphs, tomography algorithms for singleparticle coupling coefficients in several excitation number preserving models with only boundary measurement access have been proposed [13–17]—these algorithms, however, assume that all the coupling parameters in the Hamiltonian are real and positive, and thus are not applicable to many topologically nontrivial models [4,6,18,19]. Subsequent work has been done to perform tomography of spin lattices with real-valued couplings and a restricted number of probes through measurement of just the system time-traces, both for closed [20] and open quantum systems [21]. Further, the identifiability of the Hamiltonian using the protocol has also been studied to determine its applicability to various models [22,23]. Additionally, work has been done to improve the efficiency of the tomography algorithms using Bell states [24], identify one-dimensional Hamiltonians through Zeeman markers [25], perform entanglement tomography of many-body Hamiltonians [26], and use coherent states to perform tomography of quantum optical processes [27,28].

However, there still remain several experimentally relevant open questions. First, none of these protocols would be suitable for identification of topological many-body Hamiltonians, which are typically characterized by complex single-particle coupling strengths between modes to realize nonzero flux in closed loops [4,6,19]. Second, quantum simulators simulating a classically hard model necessarily have non-Gaussian terms (such as two-particle repulsion) in their Hamiltonian-it remains unclear how strengths of these non-Gaussian terms can be measured with just boundary measurement access. Finally, all the existing tomography

^{*}These authors contributed equally to this work.

[†]Contact author: rtriv@uw.edu

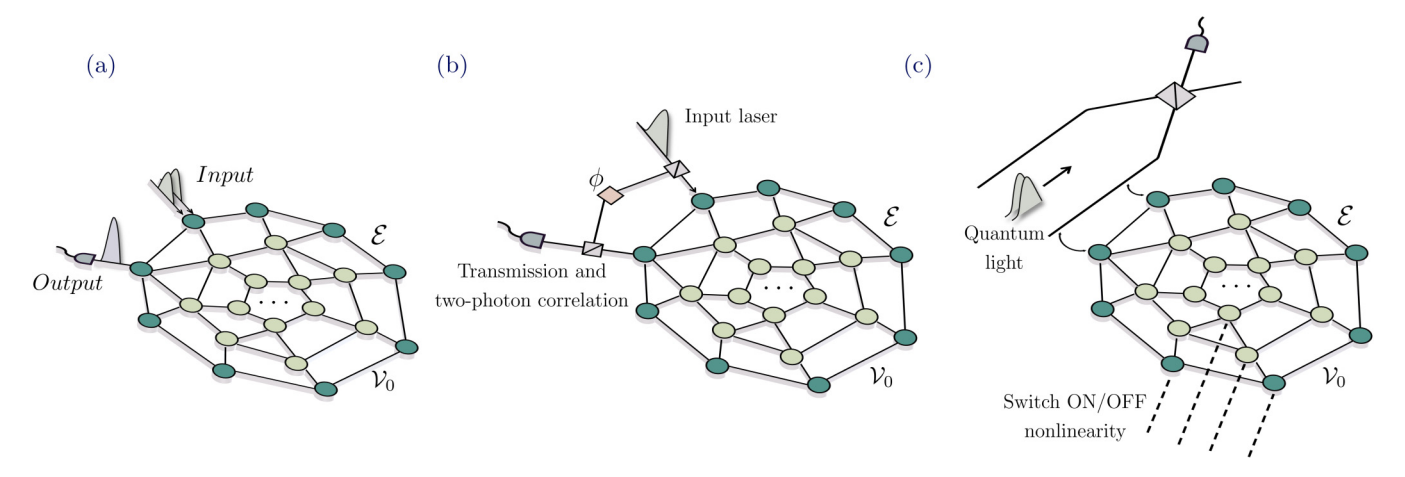


FIG. 1. (a) Schematic depicting the model of the photonic graph $(\mathcal{V}, \mathcal{E})$. The set $\mathcal{V}_0 \subseteq \mathcal{V}$ denotes the set of vertices forming the outermost boundary which are accessible to measurement. (b) Measurements used for Result 1: One of the boundary sites is excited with a weak laser and the emission from another boundary site is homodyned with the laser and then detected with either a transmission measurement or a two-photon correlation measurement. (c) Measurements used for Result 2: We excite boundary sites coupled to an arm of an interferometer with a designed Fock state or NOON state and measure the scattered photon. For this protocol, we additionally assume the ability to switch on and off the nonlinearity in the model.

algorithms achieve precision in the reconstructed Hamiltonian parameters at the standard quantum limit (SQL) [29]—it is unclear if a quantum advantage over SQL can be achieved in sensing all the Hamiltonian parameters, as can be achieved for sensing single phase or frequency parameters in the usual setting of quantum spectroscopy.

In this paper, we address all these questions in the setting where the quantum simulator can be modeled with a Bose-Hubbard Hamiltonian. This model applies to several existing quantum simulation platforms such as superconducting qubit systems and photonic quantum simulators [2,30]. By building on previous results by Burgarth et al. [15,17], which is already applicable to the Bose-Hubbard model with realvalued coupling strengths and no on-site nonlinearities, we show that both the *complex valued* single-particle couplings and on-site potentials can be reconstructed from transmission measurements. Furthermore, we show that even the on-site anharmonicity can be reconstructed from two-photon correlation function measurements from the boundary sites and under coherent-state excitation of the boundary sites. Our results are applicable to Bose-Hubbard models on graphs that satisfy the same graph infection condition that was identified and used by Burgarth et al. in Refs. [15,17]. Furthermore, we then investigate the possibility of going beyond the standard quantum limit using nonclassical excitations. By building on the protocols for quantum enhanced spectroscopy [31–34], we show that if we are able to toggle the nonlinearity in the Hamiltonian, then using multiphoton Fock state scattering from the boundaries of the lattice allows us to quantum enhance the precision in the measured Hamiltonian parameters.

II. SETUP AND SUMMARY OF RESULTS

A. Setup

We consider N bosonic modes arranged on a graph $(\mathcal{V}, \mathcal{E})$, where \mathcal{V} is the vertex set signifying the bosonic modes and \mathcal{E} are edges which signify the linear couplings between the

bosonic modes [Fig. 1(a)]. The Hamiltonian modeling this system is given by

$$H = \sum_{v \in \mathcal{V}} \left(\omega_v a_v^\dagger a_v + rac{\chi_v}{2} a_v^{\dagger 2} a_v^2
ight) + \sum_{u,v \in \mathcal{E}} J_{v,u} a_v^\dagger a_u,$$

where the parameters $J_{v,u} \in \mathbb{C}$ (the coupling strengths which also can be assumed to satisfy $J_{v,u} = J_{u,v}^*$), $\omega_v \in \mathbb{R}$ (resonant frequency), and $\chi_v \in \mathbb{R}$ (the on-site anharmonicity) need to be measured. Furthermore, in an experimentally realistic setting, each bosonic mode will also suffer from particle decay, which will impact the photon transport spectrum of the system. Including this loss, it has been previously shown [35–37] that the few-photon transport spectrum is determined by the effective non-Hermitian Hamiltonian,

$$H_{\text{eff}} = H - \frac{i}{2} \sum_{v \in \mathcal{V}} \kappa_v a_v^{\dagger} a_v$$

$$= \sum_{v \in \mathcal{V}} \left(\mu_v a_v^{\dagger} a_v + \frac{\chi_v}{2} a_v^{\dagger 2} a_v^2 \right) + \sum_{u,v \in \mathcal{E}} J_{v,u} a_v^{\dagger} a_u, \tag{1}$$

where $\mu_v = \omega_v - i\kappa_v/2$. In this case, our goal would be to reconstruct the loss rates κ_v in addition to the parameters of the lossless Hamiltonian. We point out that beyond one-particle transport, the dynamics of the system of interacting bosons is not a simple time evolution under $H_{\rm eff}$, but we have to account for Lindblad jumps. Since we use the scattering matrix formalism of Refs. [35,36] to model particle transport through this system, we account for both the non-Hermitian Hamiltonian as well as the Lindblad jumps in our analysis.

Throughout this paper, we will assume that we have boundary access to this lattice of bosonic modes. This is depicted schematically in Fig. 1: \mathcal{V}_0 is the set of vertices that correspond to the bosonic modes on the boundary of the lattice, and we will assume the ability to excite and measure the bosonic modes at these vertices. This assumption is motivated from existing experimental limitations in most

quantum hardware platforms, where setting up measurement access to every qubit is difficult [10–12].

B. Summary of results

We will consider several different kinds of boundary measurements, ranging from ones that are routinely performed in near-term experiments [Result 1, Fig. 1(b)] to those that require more careful design of the excitation and detection setup [Result 2, Fig. 1(c)]. The first case that we consider is where can excite the boundary modes with a continuous wave coherent state (e.g., a laser) and we have access to homodyne single-photon transmission (which allows us to reconstruct the parameters $J_{v,u}$, μ_v) and two-photon correlation measurements (which allows us to reconstruct the parameters χ_v) [Fig. 1(b)]. For both measurements, an input port, through which a laser excitation is applied, is coupled to a boundary site $v \in \mathcal{V}_0$ and an output port is coupled to another boundary site $u \in \mathcal{V}_0$. The input port is then excited with a continuouswave coherent state and, furthermore, the emission from the output port is interfered with the input laser field after passing it through a controllable phase shifter before being received at a photodetector.

First, we perform a transmission measurement. Here, we excite the input port with a continuous-wave coherent state at a single frequency ω and measure the intensity at the output port after homodyning. As we detail in Appendix A, it follows from photon scattering theory [35,37] that a measurement of this intensity as a function of the frequency ω as well as the homodyne phase φ allows us to extract the (complex) energies $E_{\alpha}^{(1)}$ of the effective Hamiltonian in Eq. (1) within the single-excitation subspace, as well as the parameters $M_{\alpha p}^{(1)}$,

$$M_{\alpha,v,u}^{(1)} = \langle G|a_v|r_\alpha^{(1)}\rangle\langle l_\alpha^{(1)}|a_u^\dagger|G\rangle \text{ for } v, u \in \mathcal{V}_0,$$
 (2)

where $|l_{\alpha}^{(1)}\rangle$ and $|r_{\alpha}^{(1)}\rangle$ are the left and right single-excitation eigenstates of $H_{\rm eff}^{(1)}$. The parameters $M_{\alpha,v,u}^{(1)}$ for $v,u\in\mathcal{V}_0$, contain information about the overlap of the single-excitation eigenstates of $H_{\rm eff}$ with an excitation at the boundary vertices. We remark that since we use a homodyne measurement, we are able to extract both the magnitude and phase of $M_{\alpha,v,u}^{(1)}$ —this will be key to allowing us to reconstruct potentially complex coupling coefficients $J_{v,u}$ in the model.

Next, we perform a two-particle correlation measurement. For this measurement, we use a two-tone continuous-wave coherent state with frequencies ω_1 , ω_2 through the input port and measure the two-particle correlation function at the output, after homodyning, as a function of arrival times τ_1 and τ_2 of the two photons. As we detail in Appendix A, by varying the incident frequencies ω_1 , ω_2 , the homodyned phase φ and recording the correlation function as a function of τ_1 , τ_2 , we can extract the complex energies $E_{\alpha}^{(2)}$ of the effective Hamiltonian in Eq. (1) within the two-excitation subspace, as well as the parameters $M_{\alpha,v,u}^{(2)}$,

$$M_{\bar{\alpha},v,u}^{(2)} = \langle G|a_v|r_{\alpha_1}^{(1)}\rangle\langle l_{\alpha_1}^{(1)}|a_v|r_{\alpha_2}^{(2)}\rangle\langle l_{\alpha_2}^{(2)}|a_u^{\dagger}|r_{\alpha_3}^{(1)}\rangle\langle l_{\alpha_3}^{(1)}|a_u^{\dagger}|G\rangle, \quad (3)$$

where $\vec{\alpha} = (\alpha_1, \alpha_2, \alpha_3)$ and $|l_{\alpha}^{(2)}\rangle, |r_{\alpha}^{(2)}\rangle$ are the two-excitation left and right eigenvectors of the effective Hamiltonian. Again, we emphasize that we are able to measure both the

magnitude and phase of $M^{(2)}_{\vec{\alpha},v,u}$ since we use a homodyne measurement.

In Sec. III, we build on Refs. [13-17] to provide an algorithm to reconstruct both the single-particle parameters $J_{v,u}$ and μ_v and provide an algorithm to reconstruct the two-particle parameters χ_{v} . Our algorithm works under the graph-infection assumption introduced in Ref. [17], which we briefly recap below and is schematically depicted in Fig. 2(a). Suppose that we start with the vertices in V_0 being labeled as infected, then we proceed to label another vertex $v \in \mathcal{V} \setminus \mathcal{V}_0$ as infected if it is the unique uninfected nearest neighbor of an infected vertex. The algorithm that we propose for sensing the Hamiltonian parameters will succeed if all the vertices in \mathcal{V} can be infected site by site starting from the vertices in \mathcal{V}_0 . It can be explicitly verified that several uniform lattices that are routinely encountered in quantum simulation problems, such as square, honeycomb, and triangular lattices, satisfy the graph infection condition often with only a partial boundary [Fig. 2(b)].

In Fig. 2(b), we have only considered lattices with nearest-neighbor couplings, and these satisfy the graph infection condition described above. However, in many experimental systems, there could be couplings beyond nearest-neighbors—in this case, the graph infection condition may or may not hold. For example, in Fig. 3(a), we consider a square lattice with diagonal couplings and a honeycomb lattice with next-nearest-neighbor couplings. In these cases, the lattice still satisfies the infection condition when all the boundary sites are measured. However, as shown in Fig. 3(b), there are examples in which the boundary cannot infect the whole graph after adding the next-nearest couplings. We expect that for such graphs, boundary measurements alone will not be sufficient for determining the Hamiltonian parameters uniquely, and we need to be able to measure some internal vertices as well.

Our first result can now be stated as follows:

Result 1. Consider the Bose-Hubbard model on a lattice that can be infected starting from the boundary vertices \mathcal{V}_0 , then the parameters $J_{v,u}$, μ_u , and χ_u can be reconstructed uniquely from the energy eigenvalues $E_{\alpha}^{(1)}$, $E_{\alpha}^{(2)}$, and $M_{\alpha,v,u}^{(1)}$, $M_{\bar{\alpha},v,u}^{(2)}$ with $v,u\in\mathcal{V}_0$, which can be inferred from homodyned transmission and two-particle correlation functions measured with only boundary access.

For the single-particle coupling parameters $J_{v,u}$, we go significantly beyond the algorithm in Refs. [13–17] and additionally consider lattices where the phase of the coupling coefficients $J_{v,u}$ is important, while Ref. [17] assumed that the coupling coefficients are real and positive. In particular, and as explained in Sec. III, the key step that allows us to handle complex value couplings is an identification of loops of edges between one uninfected and remaining infected nodes that allow us to fix the gauge in which the Hamiltonian parameters can be uniquely constructed. Additionally, we also provide an algorithm for the reconstruction of χ_v from two-particle correlation functions, which is an experimentally relevant setting that has not been previously explored, to the best of our knowledge.

We also numerically study the stability of our reconstruction algorithm, i.e., to what precision should the measurements at the boundary vertices be performed so as to allow for

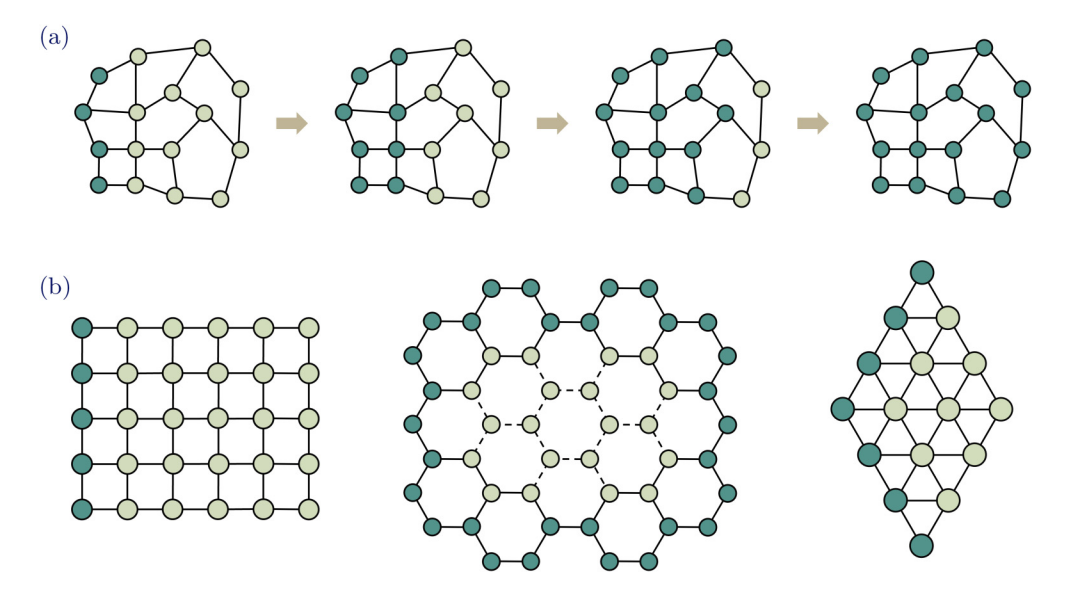


FIG. 2. (a) Schematic illustration of the graph infection condition—the vertices with measurement access, shown in a dark green color, are assumed to be initially infected. These vertices then infect their unique nearest neighbors—the graphs that we consider in this paper should be such that, proceeding this way, all the vertices can be infected. (b) Examples of graphs, as well as choice of boundary vertices (i.e., initially infected vertices) that satisfy the graph infection condition.

a certain target precision in the reconstructed parameters? The precision required at the boundary measurement would then set the number of repetitions of the measurement that needs to be performed or, alternatively, the number of exciting photons that need to be used—in particular, to perform a boundary measurement of the transmission or the correlation function to a precision δ , we would need $O(\delta^{-2})$ photons or measurement trials. For the tomography algorithm to be efficient and scalable, it is desirable that required measurement precision scales at most poly(N) with the number of sites. Through our numerical studies, we find that for models with delocalized single and two-particle eigenstates, the required measurement precision to determine $J_{v,u}$ and μ_v only scales polynomially with the number of sites N, while it scales exponentially with N if the target is to determine χ_{ν} to a target precision. This potentially limits our algorithm for reconstructing χ_{ν} to small system sizes—however, this can be remedied in platforms where it is possible to switch the nonlinearity χ_v on each site on and off, and we display a simple algorithm that utilizes this additional control to stably find χ_{ν} . Section III provides a detailed description of this algorithm, together with numerical studies of its stability for some paradigmatic examples.

Next, we consider the question of a possible quantum enhancement of the precision with which the parameters of the Hamiltonian can be measured. The tomography algorithm described thus far, for a fixed number of sites N, only obtains a precision constrained by the standard quantum limit, i.e., to determine the coefficients in the Hamiltonian to a precision ε would require $O(\varepsilon^{-2})$ photons—this is simply due to the fact that the photons are used independently while performing the measurement. We then investigate the question of improving the dependence of the number of photons on the target precision ε beyond the standard quantum limit by using all the photons in parallel. Here, as depicted in Fig. 1(c), we assume the ability to switch on and off the on-site two-particle repulsion term in the Hamiltonian and adapt methods used in quantum-enhanced spectroscopy [31–34] to show the following result.

Result 2. Consider the Bose-Hubbard model on a lattice that satisfies assumption 1 and assume the ability to switch

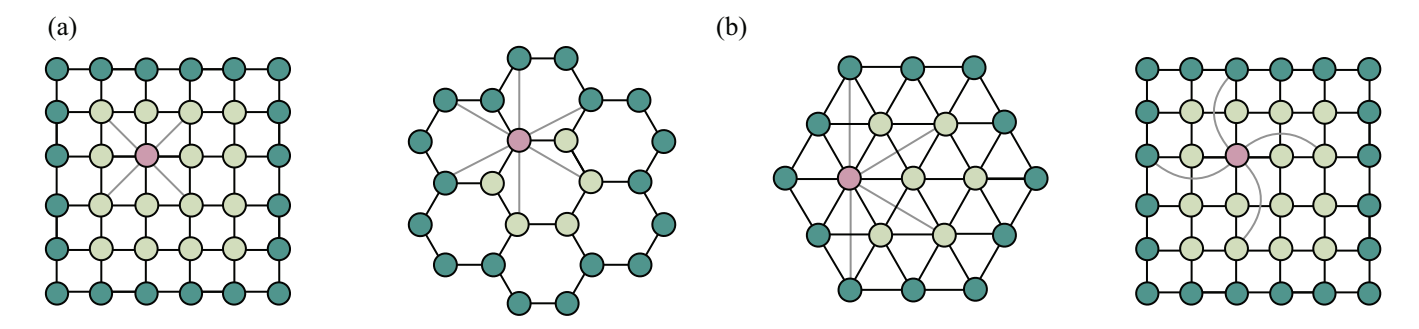


FIG. 3. (a) Examples of lattices with nearest- (black) and next-nearest- (grey) neighbor couplings, where boundary measurement is sufficient to infect the full graph. (b) Examples in which the graph does not satisfy the infection condition after adding next-nearest-neighbor couplings. We only illustrate the next-nearest couplings for a single site for clarity, but this should be considered to exist at all sites.

on and off the nonlinear term in the model. Then, for a fixed lattice size N, the parameters $J_{v,u}$ and μ_u can be reconstructed to a precision ε with $O(\varepsilon^{-1})$ photons and only using boundary measurements. Furthermore, χ_u can be reconstructed to a precision of ε with $O(\varepsilon^{-2/3})$ photons and only using boundary measurements.

Sec. IV, we detail the reconstruction protocol. We point out that while the result here builds on well-known quantum-enhanced spectroscopy protocols, such as twin-Fock state spectroscopy [32,33] and NOON state spectroscopy [34], these protocols usually sense a single and easily accessible system parameter (e.g., a single phase shift or a frequency). Our key contribution is to utilize and extend these techniques to enhance the precision of all the Hamiltonian parameters while only being able to excite and measure the lattice through the boundary vertices.

We also point out that while we attain a Heisenberg scaling [i.e., $O(\varepsilon^{-1})$] in the number of photons required for reconstruction of the single-particle parameters $J_{v,u}$ and μ_u , we obtain a super Heisenberg scaling [i.e., slower than $O(\varepsilon^{-1})$] in the number of photons required for the reconstruction of χ_{ν} . Such a super-Heisenberg scaling is not surprising or unphysical, and has been previously obtained for sensing problems with a many-body probe with all-to-all interactions [38.39], as well as for the problem of sensing nonlinearity in a single anharmonic oscillator [40]. As analyzed in Ref. [40], this super-Heisenberg scaling arises from the fact that if a single anharmonic oscillator with $H = \chi a^{\dagger 2} a^2/2$ is initialized in the P photon state $|P\rangle \propto a^{\dagger P}|0\rangle$, then after time t, this state acquires a phase $\propto \chi P^2 t$ that scales quadratically with P. Thus, if we are able to measure this phase to a constant precision, then to obtain a precision ε in χ , we simply need to choose $P \sim \varepsilon^{-1/2}$. The problem of measuring χ_v in the Bose-Hubbard model, however, is more involved since the photons at any one oscillator can also interact with other oscillators, and consequently we don't accumulate a simple phase on time evolution that can be measured later. However, as detailed in Sec. IV, this unwanted interaction can be suppressed by choosing a sufficiently short evolution time while still retaining a super-Heisenberg scaling of the required number of photons with the target precision in χ_v .

III. TOMOGRAPHY WITH SINGLE AND TWO-PARTICLE MEASUREMENTS

In this section, we provide details of the tomography algorithm corresponding to Result 1. We perform the tomography in two steps: First, we consider reconstruction of only the single-particle parameters $J_{v,u}$ and μ_v from the measurements of the single-excitation eigenenergies $E_{\alpha}^{(1)}$ and $M_{\alpha,v,u}^{(1)}$. Having determined these parameters, we then reconstruct the two-particle parameters χ_v . Finally, we will provide a numerical study of the stability of the tomography algorithm.

A. Reconstructing the single-particle parameters $J_{v,u}$, μ_v

In the first stage of the scheme, we use $M_{\alpha,v,u}^{(1)} \,\forall v, u \in \mathcal{V}_0$ and eigenenergies $E_{\alpha}^{(1)}$ extracted from boundary transmission measurements to reconstruct the single-particle parameters

 $J_{v,u}$ and μ_v . As schematically shown in Fig. 4 and similar to Ref. [13], the idea behind the reconstruction procedure is to keep track of a set of infected vertices \mathcal{I} and compute the Hamiltonian parameters corresponding to the infected vertices, i.e., μ_v and $J_{v,u}$ for $v, u \in \mathcal{I}$. The set of infected vertices is initially taken to be the boundary (\mathcal{V}_0) , and we sequentially add uninfected vertices to this set till the full lattice has been covered. We emphasize that the infected vertices includes vertices in the bulk of the lattice (i.e., not in the boundary V_0) in the intermediate steps of the reconstruction procedure. In particular, at any stage of the reconstruction procedure, we will define the set of infected vertices \mathcal{I} to be such that $M_{\alpha,v,u}^{(1)}$ is known for all $v, u \in \mathcal{I}$ such that the edge (v, u) exists. For ease of notation, we define by \mathcal{E}_I the set of edges in the Hamiltonian graph that involve vertices in \mathcal{I} , i.e., $\mathcal{E}_I = \{(v, u) \in \mathcal{E} | v, u \in \mathcal{I}\}$. At the start of the reconstruction procedure, by assumption we have that the infected set of vertices is the boundary set $(\mathcal{I} = \mathcal{V}_0)$. With this data together with the eigenenergies $E_{\alpha}^{(1)}$, we can then determine $\mu_v \in \mathcal{I}$ and $J_{v,u}$ for $(v, u) \in \mathcal{E}_I$. This can be determined straightforwardly from the eigenvalue equation corresponding to $H_{\rm eff}$ within the single excitation subspace [8]. More concretely, since $H_{\text{eff}}|r_{\alpha}^{(1)}\rangle = E_{\alpha}^{(1)}|r_{\alpha}^{(1)}\rangle$ and $\langle l_{\alpha}^{(1)}|H_{\text{eff}} = E_{\alpha}^{(1)}\langle l_{\alpha}^{(1)}|$, we have

$$E_{\alpha}^{(1)}\langle G|a_{v}\big|r_{\alpha}^{(1)}\rangle = \mu_{v}\langle G|a_{v}\big|r_{\alpha}^{(1)}\rangle + \sum_{v'\in\mathcal{N}_{v}} J_{v,v'}\langle G|a_{v'}\big|r_{\alpha}^{(1)}\rangle, \tag{4a}$$

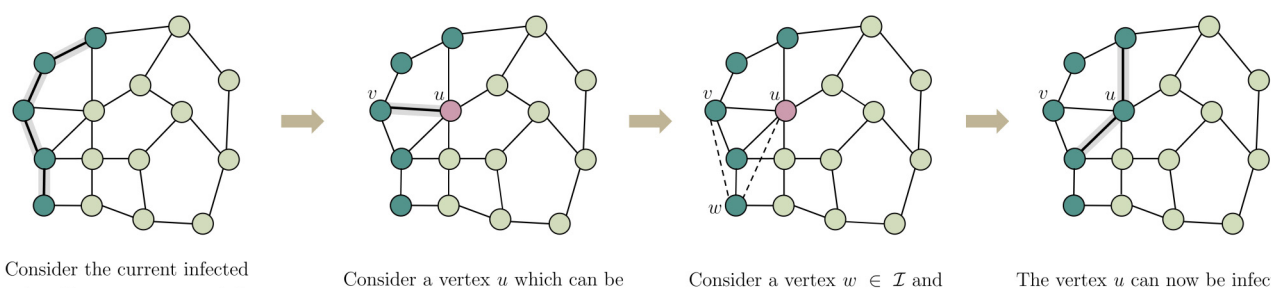
$$E_{\alpha}^{(1)}\langle l_{\alpha}^{(1)}\big|a_{v}^{\dagger}|G\rangle = \mu_{v}\langle l_{\alpha}^{(1)}\big|a_{v}^{\dagger}|G\rangle + \sum_{v'\in\mathcal{N}_{v}} J_{v',v}\langle l_{\alpha}^{(1)}\big|a_{v'}^{\dagger}|G\rangle, \tag{4b}$$

where \mathcal{N}_v is the deleted neighborhood of the vertex v, i.e., it is the set of vertices other than v that share an edge with v. Using the completeness of $|I_{\alpha}^{(1)}\rangle, |r_{\alpha}^{(1)}\rangle, \sum_{\alpha} |I_{\alpha}^{(1)}\rangle\langle r_{\alpha}^{(1)}| = I^{(1)}$ (where $I^{(1)}$ is the identity within the single-excitation subspace), we obtain from this equation that for every $v \in \mathcal{I}$ and $(v, u) \in \mathcal{E}_I$:

$$\mu_v = \sum_{\alpha} E_{\alpha}^{(1)} M_{\alpha,v,v}^{(1)} \text{ and } J_{v,u} = \sum_{\alpha} E_{\alpha}^{(1)} M_{\alpha,v,u}^{(1)}.$$
 (5)

Next, consider a vertex $u \in \mathcal{V} \setminus \mathcal{I}$ in the bulk that is uninfected but can be infected by the vertices in \mathcal{I} . By definition, this means that u is a unique uninfected nearest neighbor of an infected vertex $v \in \mathcal{I}$. First, we consider the coupling $J_{v,u}$ —we can assume this coupling to be real and positive. We can accomplish this because gauge freedom allows us to alter the phases of annihilation operators, denoted by $a_k \to a_k e^{i\varphi_k}$ for $k \in \mathcal{V}$, and coupling rates, represented by $J_{k,l} \to J_{k,l} e^{i(\varphi_k - \varphi_l)}$ for $(k, l) \in \mathcal{E}$, where φ_k and φ_l are arbitrary phases. Consequently, the phases of coupling rates are not physical quantities; they depend on the chosen gauge. However, the sum of coupling rate phases within any closed loop in the graph remains unchanged and is invariant. Therefore, assuming $J_{v,u}$ to be real and positive amounts to fixing the local gauge of the bosonic mode at site u, which has not been fixed as of yet. Now, we can rewrite Eqs. (4) as

$$\begin{split} J_{v,u}\langle G|a_u\big|r_\alpha^{(1)}\big\rangle &= \big(E_\alpha^{(1)}-\mu_v\big)\langle G|a_v\big|r_\alpha^{(1)}\big\rangle \\ &-\sum_{v'\in\mathcal{N}_v\setminus\{u\}}J_{v,v'}\langle G|a_{v'}\big|r_\alpha^{(1)}\big\rangle \text{ and } \quad \text{(6a)} \end{split}$$



Consider the current infected vertices \mathcal{I} - compute μ_v and $J_{v,u}$ corresponding to these vertices from $E_{\alpha}^{(1)}$ and $M_{\alpha,v,u}^{(1)}$, which is known for $v, u \in \mathcal{I}$ by definition of \mathcal{I} .

Consider a vertex u which can be infected by a vertex $v \in \mathcal{I}$. Calculate $J_{v,u}, M_{\alpha,u,u}^{(1)}, M_{\alpha,v,u}^{(1)}, M_{\alpha,u,v}^{(1)}$ from the corresponding data for the infected vertices.

Consider a vertex $w \in \mathcal{I}$ and compute $M_{\alpha,u,w}^{(1)}, M_{\alpha,w,u}^{(1)}$ by identifying the cyclical relation between v, u and w.

The vertex u can now be infected and added to the set \mathcal{I} . Compute $J_{v,u}$ for edges corresponding to the updated \mathcal{I} and repeat these steps for the next vertex which can be infected.

FIG. 4. Schematic depicting the tomography algorithm in the single-excitation space. The dark-green vertices are the currently infected vertices, while the red vertex is the vertex being infected.

$$J_{v,u}\langle l_{\alpha}^{(1)} | a_{u}^{\dagger} | G \rangle = \left(E_{\alpha}^{(1)} - \mu_{v} \right) \langle l_{\alpha}^{(1)} | a_{v}^{\dagger} | G \rangle$$
$$- \sum_{v' \in \mathcal{N}_{\sim} \setminus \{u\}} J_{v,v'}^{*} \langle l_{\alpha}^{(1)} | a_{v'}^{\dagger} | G \rangle, \tag{6b}$$

where we have used that $J_{v,u}$ is real and $J_{v,v'} = J_{v',v}^*$. Multiplying these equations and summing over α , we obtain that

$$J_{v,u}^{2} = \sum_{\alpha} \left(E_{\alpha}^{(1)} - \mu_{v} \right)^{2} M_{\alpha,v,v}^{(1)} - \sum_{v' \in \mathcal{N}_{v} \setminus \{u\}} |J_{v,v'}|^{2}. \tag{7}$$

$$M_{\alpha,u,u}^{(1)} = \frac{\left(E_{\alpha}^{(1)} - \mu_{v}\right)}{J_{v,u}^{2}} \left[\left(E_{\alpha}^{(1)} - \mu_{v}\right) M_{\alpha,v,v}^{(1)} - \sum_{v' \in \mathcal{N}_{v} \setminus \{u\}} \left(J_{v,v'} M_{\alpha,v,v'}^{(1)} + J_{v,v'}^{*} M_{\alpha,v',v}^{(1)}\right) \right] + \sum_{v'_{1},v'_{2} \in \mathcal{N}_{v} \setminus \{u\}} \frac{J_{v,v'_{1}} J_{v,v'_{2}}^{*}}{J_{v,u}^{2}} M_{\alpha,v'_{1},v'_{2}}^{(1)}.$$
(8a)

Furthermore, multiplying Eq. (6a) by $\langle l_{\alpha}^{(1)}|a_v|G\rangle$ and Eq. (6b) by $\langle G|a_v|r_{\alpha}^{(1)}\rangle$ allows us to determine $M_{\alpha,u,v}^{(1)}$ and $M_{\alpha,v,u}^{(1)}$, respectively, via

$$M_{\alpha,u,v}^{(1)} = \frac{1}{J_{v,u}} \left(\left(E_{\alpha}^{(1)} - \mu_v \right) M_{\alpha,v,v}^{(1)} - \sum_{v' \in \mathcal{N}_v \setminus \{u\}} J_{v,v'} M_{\alpha,v',v}^{(1)} \right), \tag{8b}$$

$$M_{\alpha,v,u}^{(1)} = \frac{1}{J_{v,u}} \bigg(\big(E_{\alpha}^{(1)} - \mu_v \big) M_{\alpha,v,v}^{(1)} - \sum_{v' \in \mathcal{N}_v \setminus \{u\}} J_{v,v'}^* M_{\alpha,v,v'}^{(1)} \bigg).$$
(8c)

It can be noted that the right-hand sides of all the equations in Eqs. (8) can be evaluated since $J_{v,u}$ is known, and v as well as the vertices in $\mathcal{N}_v \setminus \{u\}$ are in \mathcal{I} .

Next, we show that vertex u can now be added to the set of infected vertices \mathcal{I} . For this, we need to compute $M_{\alpha,u,w}^{(1)}$ and $M_{\alpha,w,u}^{(1)}$ for all $w \in \mathcal{I}$. This can be done by utilizing the following simple cyclic relationship: Consider a vertex $w \in \mathcal{I}$, the vertex $v \in \mathcal{I}$ which is a neighbor of u, and the vertex u, then

$$M_{\alpha,u,w}^{(1)} = \frac{M_{\alpha,u,v}^{(1)} M_{\alpha,v,w}^{(1)}}{\left(M_{\alpha,v,v}^{(1)}\right)^*} \quad \text{and} \quad M_{\alpha,w,u}^{(1)} = \frac{M_{\alpha,w,v}^{(1)} M_{\alpha,v,u}^{(1)}}{M_{\alpha,v,v}^{(1)}}.$$

$$(9)$$

Since $M_{\alpha,v,w}^{(1)}, M_{\alpha,w,v}^{(1)}$, and $M_{\alpha,v,v}^{(1)}$ are known, this allows us to determine $M_{\alpha,u,w}^{(1)}$ for all $w \in \mathcal{I}$. Now, vertex u can also treated as an infected vertex and added to set \mathcal{I} . Then, using Eq. (6),

once $J_{v,u}$ have been determined, we can again use Eq. (6) to determine $M_{\alpha,u,u}^{(1)}$, $M_{\alpha,v,u}^{(1)}$, and $M_{\alpha,u,v}^{(1)}$. In particular, $M_{\alpha,u,u}^{(1)}$ can be determined by multiplying Eq. (6):

Note that $J_{v,u}$ is positive, and that $J_{v,v'}$ for all $v' \in \mathcal{N}_v \setminus \{u\}$ are known. This is so because u is the only uninfected neighbor of

v; consequently, the set vertices in $\mathcal{N}_v \setminus \{u\}$ are already in \mathcal{I} . Therefore, $J_{v,u}$ can be determined from Eq. (7). Furthermore,

we can compute the single-particle couplings between u and other sites in \mathcal{I} .

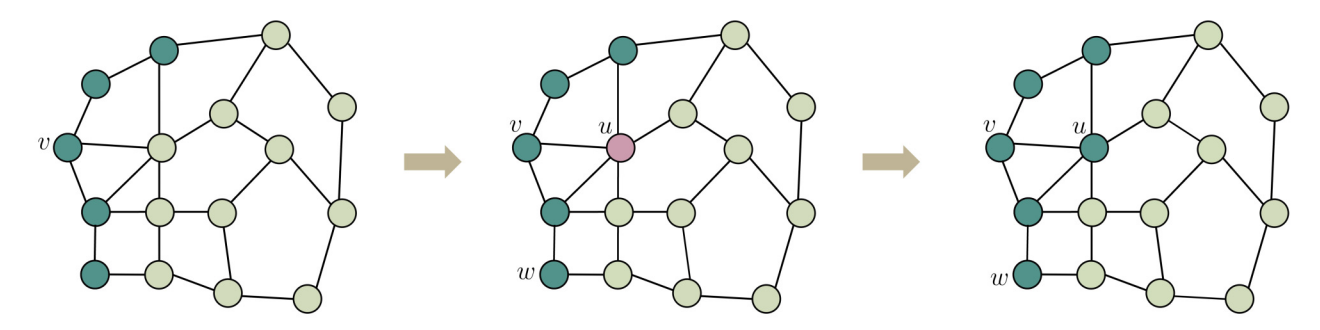
Next, we repeat this entire process with another uninfected vertex that can be infected by \mathcal{I} . Our assumption on the graph is that they can be entirely infected starting from the initial $\mathcal{I} = \mathcal{V}_0$ and therefore all the Hamiltonian parameters can be reconstructed.

B. Reconstructing χ

The second stage involves working in two-photon space, and using the determined single-particle Hamiltonian $H^{(1)}$ along with the measured values of $M_{\vec{\alpha},v,u}^{(2)}$, where $\vec{\alpha}=(\alpha_1,\alpha_2,\alpha_3)$ and $v,u\in\mathcal{V}_0$, to calculate $\chi_v\ \forall\ v\in\mathcal{V}$ and hence mapping the full Hamiltonian H. As with the reconstruction of the single-particle parameters, we will develop a recursive algorithm to reconstruct χ_v for graphs in which all vertices can be infected by the vertices at the boundary. The recursion is more naturally formulated in terms of the coefficients $C_{\vec{\alpha},v,u}^{(2)}, Q_{\vec{\alpha},v,u}^{(2)}, R_{\vec{\alpha},v,u}^{(2)}$, which are defined by

$$\begin{split} C_{\vec{\alpha},v,u}^{(2)} &= \big\langle l_{\alpha_{1}}^{(1)} \big| a_{v} \big| r_{\alpha_{2}}^{(2)} \big\rangle \big\langle l_{\alpha_{2}}^{(2)} \big| a_{u}^{\dagger} \big| r_{\alpha_{3}}^{(1)} \big\rangle, \\ Q_{\vec{\alpha},v,u}^{(2)} &= \big\langle l_{\alpha_{1}}^{(1)} \big| a_{v}^{\dagger} a_{v}^{2} \big| r_{\alpha_{2}}^{(2)} \big\rangle \big\langle l_{\alpha_{2}}^{(2)} \big| a_{u}^{\dagger} \big| r_{\alpha_{3}}^{(1)} \big\rangle, \\ R_{\vec{\alpha},v,u}^{(2)} &= \big\langle l_{\alpha_{1}}^{(1)} \big| a_{v} \big| r_{\alpha_{2}}^{(2)} \big\rangle \big\langle l_{\alpha_{2}}^{(2)} \big| (a_{u}^{\dagger})^{2} a_{u} \big| r_{\alpha_{3}}^{(1)} \big\rangle. \end{split}$$

We note that if the single-particle parameters, $J_{v,u}$ and μ_v , have already been reconstructed, which in turn allows us to compute the single-particle eigenstates $|r_{\alpha}^{(1)}\rangle$, $|l_{\alpha}^{(1)}\rangle$, then



Consider the current infected vertices \mathcal{I} - compute χ_v using $C_{\vec{\alpha},v,u}^{(2)}$, which is known for $v,u\in\mathcal{I}$ by definition of \mathcal{I} .

Consider a vertex $u \notin \mathcal{I}$ which can be infected by a vertex $v \in \mathcal{I}$.

Calculate $C^{(2)}_{\vec{\alpha},u,w}$ and $C^{(2)}_{\vec{\alpha},w,u}$ from the corresponding data for the infected vertices.

The vertex u can now be infected and added to the set \mathcal{I} . Compute χ_u and repeat these steps for the next vertex which can be infected.

FIG. 5. Schematic depicting the tomography algorithm in the two-excitation space. The dark-green vertices are the currently infected vertices, while the red vertex is the vertex being infected.

 $C^{(2)}_{\vec{\alpha},v,u}, Q^{(2)}_{\vec{\alpha},v,u}, R^{(2)}_{\vec{\alpha},v,u}$, for $v, u \in \mathcal{V}_0$, can be determined from $M^{(2)}_{\vec{\alpha},v,u}$ obtained from the boundary measurements. It is straightforward to see this for $C^{(2)}_{\vec{\alpha},v,u}$ since

$$C_{\vec{a},v,u}^{(2)} = \frac{M_{\vec{a},v,u}^{(2)}}{\langle G|a_v|r_{\alpha_1}^{(1)}\rangle \langle l_{\alpha_3}^{(1)}|a_u^{\dagger}|G\rangle}.$$

Furthermore, we use the completeness of $|r_{\alpha}^{(1)}\rangle, |l_{\alpha}^{(1)}\rangle$ in the single-excitation subspace to express $Q_{\vec{\alpha},v,u}^{(2)}$ and $R_{\vec{\alpha},v,u}^{(2)}$ in terms of $C_{\vec{\alpha},v,u}^{(2)}$ via

$$Q_{\vec{\alpha},v,u}^{(2)} = \sum_{\alpha'} \langle l_{\alpha_1}^{(1)} | a_v^{\dagger} a_v | r_{\alpha_1'}^{(1)} \rangle C_{(\alpha_1',\alpha_2,\alpha_3),v,u}^{(2)},$$
(10a)

$$R_{\vec{\alpha},v,u}^{(2)} = \sum_{\alpha_3'} \langle l_{\alpha_3'}^{(1)} | a_u^{\dagger} a_u | r_{\alpha_3}^{(1)} \rangle C_{(\alpha_1,\alpha_2',\alpha_3),v,u}^{(2)}.$$
 (10b)

Similar to the previous subsection and as shown in Fig. 5, at any stage of the reconstruction algorithm, we define the set of *infected vertices* $\mathcal I$ as the vertices v,u such that $C^{(2)}_{\vec\alpha,v,u}$ and $C^{(2)}_{\vec\alpha,u,v}$ are known for all $v,u\in\mathcal I$ and for all $\vec\alpha$. At the start of the algorithm, $\mathcal I$ coincides with the boundary vertices $\mathcal V_0$. To develop the reconstruction algorithm, we will use the eigenvalue equation for $H_{\rm eff}$ in the two-excitation subspace: $H_{\rm eff}|r^{(2)}_{\alpha_2}\rangle = E^{(2)}_{\alpha_2}|r^{(2)}_{\alpha_2}\rangle$ and $\langle l^{(2)}_{\alpha_2}|H_{\rm eff}=E^{(2)}_{\alpha_2}\langle l^{(2)}_{\alpha_2}|$. Multiplying the right eigenvector equation by $a^\dagger_v|r^{(1)}_{\alpha_3}\rangle$, we obtain

$$\begin{split} &\chi_{v}\langle l_{\alpha_{1}}^{(1)} \big| a_{v}^{\dagger} a_{v}^{2} \big| r_{\alpha_{2}}^{(2)} \rangle + \sum_{v' \in \mathcal{N}_{v}} J_{v,v'} \langle l_{\alpha_{1}}^{(1)} \big| a_{v'} | r_{\alpha_{2}}^{(2)} \rangle \\ &= \left(E_{\alpha_{2}}^{(2)} - \mu_{v} - E_{\alpha_{1}}^{(1)} \right) \langle l_{\alpha_{1}}^{(1)} \big| a_{v} \big| r_{\alpha_{2}}^{(2)} \rangle = 0, \\ &\chi_{v} \langle l_{\alpha_{2}}^{(2)} \big| a_{v}^{\dagger 2} a_{v} \big| r_{\alpha_{3}}^{(1)} \rangle + \sum_{v' \in \mathcal{N}_{v}} J_{v',v} \langle l_{\alpha_{2}}^{(2)} \big| a_{v'}^{\dagger} \big| r_{\alpha_{3}}^{(1)} \rangle \end{split}$$
(11a)

$$+ \left(E_{\alpha_2}^{(2)} - \mu_v - E_{\alpha_3}^{(1)}\right) \langle I_{\alpha_2}^{(2)} | a_v^{\dagger} | r_{\alpha_3}^{(1)} \rangle = 0.$$
 (11b)

From these eigenvalue equations, we can now obtain χ_v for $v \in \mathcal{I}$. First, we note that since $|r_{\alpha}^{(1)}\rangle, |l_{\alpha}^{(1)}\rangle$, and $|r_{\alpha}^{(2)}\rangle, |l_{\alpha}^{(2)}\rangle$ are complete within the first and second excitation subspaces,

respectively:

$$\sum_{\alpha_1,\alpha_2} \langle l_{\alpha_1}^{(1)} | a_v | r_{\alpha_2}^{(2)} \rangle \langle l_{\alpha_2}^{(2)} | a_u^{\dagger} | r_{\alpha_1}^{(1)} \rangle = 2\delta_{v,u}.$$

Then, multiplying Eq. (11a) by $\langle l_{\alpha_2}^{(2)}|a_u^\dagger|r_{\alpha_1}^{(1)}\rangle$ and summing over the indices α_1 , α_2 , we obtain that

$$\chi_v = -\frac{1}{2} \sum_{\alpha_1,\alpha_2} \left(\mu_v + E_{\alpha_1}^{(1)} - E_{\alpha_2}^{(2)} \right) C_{(\alpha_1,\alpha_2,\alpha_1),v,v}^{(2)}. \tag{12}$$

If $v \in \mathcal{I}$, then the right-hand side of Eq. (12) is completely known, and thus χ_v can be reconstructed.

Next, we consider a vertex $u \in \mathcal{V} \setminus \mathcal{I}$ and can be infected by a vertex in \mathcal{I} . By definition, this implies that u is the *unique uninfected nearest neighbor* of a vertex $v \in \mathcal{I}$ [Fig. 5]. In what follows, we show that the vertex u can be added to the set of infected vertices \mathcal{I} since we can determine $C_{\overline{\alpha},w,u}^{(2)}$ and $C_{\overline{\alpha},u,w}^{(2)}$ for all $w \in \mathcal{I}$. First, consider determining $C_{\overline{\alpha},u,w}^{(2)}$ — this can be done multiplying Eq. (11a) by $\langle l_{\alpha_2}^{(2)} | a_w^{\dagger} | r_{\alpha_3}^{(1)} \rangle$ to obtain

$$\begin{split} C^{(2)}_{\vec{\alpha},u,w} &= \frac{1}{J_{v,u}} \Biggl(\bigl(E^{(2)}_{\alpha_2} - \mu_v - E^{(1)}_{\alpha_1} \bigr) C^{(2)}_{\vec{\alpha},v,w} \\ &- \sum_{v' \in \mathcal{N}_v \setminus \{u\}} J_{v,v'} C^{(2)}_{\vec{\alpha},v',w} - \chi_v Q^{(2)}_{\vec{\alpha},v,w} \Biggr). \end{split}$$

Observe that, from this equation, the evaluation of $C^{(2)}_{\vec{\alpha},u,w}$ requires the coefficients $C^{(2)}_{\vec{\alpha},v_1,v_2}, Q^{(2)}_{\vec{\alpha},v_1,v_2}$ for only infected vertices $v_1, v_2 \in \mathcal{I}$. $C^{(2)}_{\vec{\alpha},v_1,v_2}$ is known by definition and $Q^{(2)}_{\vec{\alpha},v_1,v_2}$ can be obtained using Eq. (10). A similar procedure can be followed to obtain $C^{(2)}_{\vec{\alpha},w,u}$. Multiplying Eq. (11b) by $\langle l^{(1)}_{\alpha_1}|a_w|r^{(2)}_{\alpha_2}\rangle$, we obtain

$$C_{\vec{\alpha},w,u}^{(2)} = \frac{1}{J_{u,v}} \left(\left(E_{\alpha_2}^{(2)} - \mu_v - E_{\alpha_1}^{(1)} \right) C_{\vec{\alpha},w,v}^{(2)} - \sum_{v' \in \mathcal{N}_v \setminus \{u\}} J_{v',v} C_{\vec{\alpha},w,v'}^{(2)} - \chi_v R_{\vec{\alpha},w,v}^{(2)} \right),$$

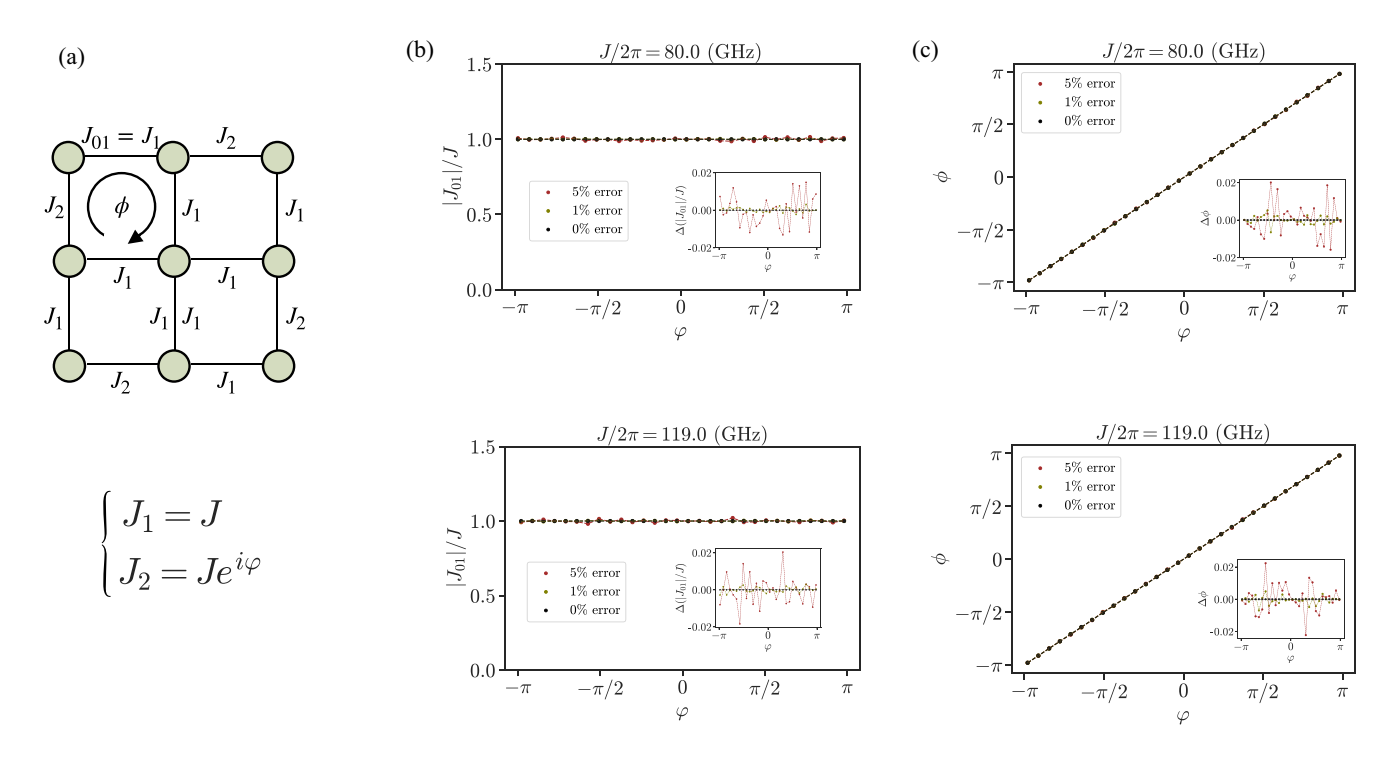


FIG. 6. (a) Schematic depiction of the lattice example featuring real coupling coefficients J_1 and complex-valued J_2 . Here, ϕ denotes the invariant phase within the designated loop, while J_{01} signifies the coupling strength between nodes 0 and 1. (b) Reconstruction of $|J_{01}|$ as a function of φ for different values of J. The measurement values for the parameters $M_{\alpha,\nu,u}^{(1)}$ are assumed to have error rates of 0, 1%, and 5%. Each data point is averaged over 50 distinct samples for measurement error. (c) Reconstruction of φ as a function of φ for different values of J.

where gain involves only coefficients $C_{\vec{a},v_1,v_2}^{(2)}$ and $R_{\vec{a},v_1,v_2}^{(2)}$ corresponding to infected vertices $v_1, v_2 \in \mathcal{I}$, and thus can be entirely determined using the known $C_{\vec{a},v_1,v_2}^{(2)}$ and Eq. (10). Since we have successfully determined both $C_{\vec{a},u,w}^{(2)}$ and $C_{\vec{a},w,u}^{(2)}$ for all $w \in \mathcal{I}$, we can add vertex u to the set of infected vertices. Then, we can go on to determine χ_u using Eq. (12) and repeat this process until all vertices have been infected, and thus all the on-site anharmonicities have been determined.

C. Impact of measurement errors

In the last two subsections, our analysis assumed that the measurements are perfect, i.e., the boundary data $E_{\alpha}^{(1)}, E_{\alpha}^{(2)}, M_{\alpha,v,u}^{(1)}$, and $M_{\bar{\alpha},v,u}^{(2)}$ are known perfectly. However, in an experimentally realistic setting, there will be an error in the measured data—this raises the question of how much the reconstructed Hamiltonian parameters diverge from true ones when measurements contain errors. The primary inputs into the algorithm are the eigenenergies $E_{\alpha}^{(1)}, E_{\alpha}^{(2)}$ and the coefficients $M_{\alpha,v,u}^{(1)}, M_{\bar{\alpha},v,u}^{(2)}$ (or, alternatively, $C_{\bar{\alpha},v,u}^{(2)}$). In a well-calibrated experimental setup, it is reasonable to assume that the eigenenergies can be determined to an accuracy that is much higher than the eigenvector overlaps since the eigenenergies can be determined entirely through the position of the resonances. Hence, in this section, we focus on determining scaling of the error in the reconstructed couplings with the error in the coefficients.

Before investigating the error scaling with the increasing number of sites N, we first verify the algorithm's validity

through a simple example, as depicted in Fig. 6. We examine the reconstruction of the invariant phase of a loop, ϕ , and the magnitude of a hopping rate J_{01} , both specified in Fig. 6. As anticipated, the algorithm accurately identifies these values in the absence of errors in the measurement coefficients $M_{\alpha,\nu,u}^{(1)}$; however, deviations begin to emerge as we introduce measurement errors. To illustrate how the error scales with increasing N, we take up the Su-Schrieffer-Heeger (SSH) model [41] which can be described by the Hamiltonian

$$H_{\text{SSH}} = \sum_{v} (t_1 a_{2v+1}^{\dagger} a_{2v} + t_2 a_{2v+2}^{\dagger} a_{2v+1} + \text{H.c.}),$$

where each site of the lattice has the same on-site potential μ_0 , but the couplings alternate between t_1 , t_2 . For a small error $\delta M_{\alpha,v,u}^{(1)}$, $\delta C_{\bar{\alpha},v,u}^{(2)}$, the errors in the reconstructed coefficients $J_{v,u}$ and χ_v can be approximated by

$$\delta J_{v,u} = \sum_{\alpha,v',u'} \frac{\partial J_{v,u}}{\partial M_{\alpha,v',u'}^{(1)}} \delta M_{\alpha,v',u'}^{(1)},$$

$$\delta \chi_v = \sum_{\vec{\alpha},v,u} \left(\frac{\partial \chi_v}{\partial C_{\vec{\alpha},v',u'}^{(2)}} \delta C_{\vec{\alpha},v',u'}^{(2)} + \frac{\partial \chi_v}{\partial J_{v',u'}} \delta J_{v',u'} \right).$$

Further, we assume that errors in the coefficients are uncorrelated, i.e., $\langle \delta M^{(1)}_{\alpha,v,u} \delta M^{(1)}_{\alpha',v',u'} \rangle = \delta_{\alpha,\alpha'} \delta_{v,v'} \delta_{u,u'},$ $\langle \delta C^{(2)}_{\vec{\alpha},v,u} \delta C^{(2)}_{\vec{\alpha}',v',u'} \rangle = \delta_{\vec{\alpha},\vec{\alpha'}} \delta_{v,v'} \delta_{u,u'},$ and $\langle \delta M^{(1)}_{\alpha,v,u} \delta C^{(2)}_{\vec{\alpha},v,u} \rangle = 0$, which is a reasonable assumption to make since we are dealing with errors at different frequencies, and we can then

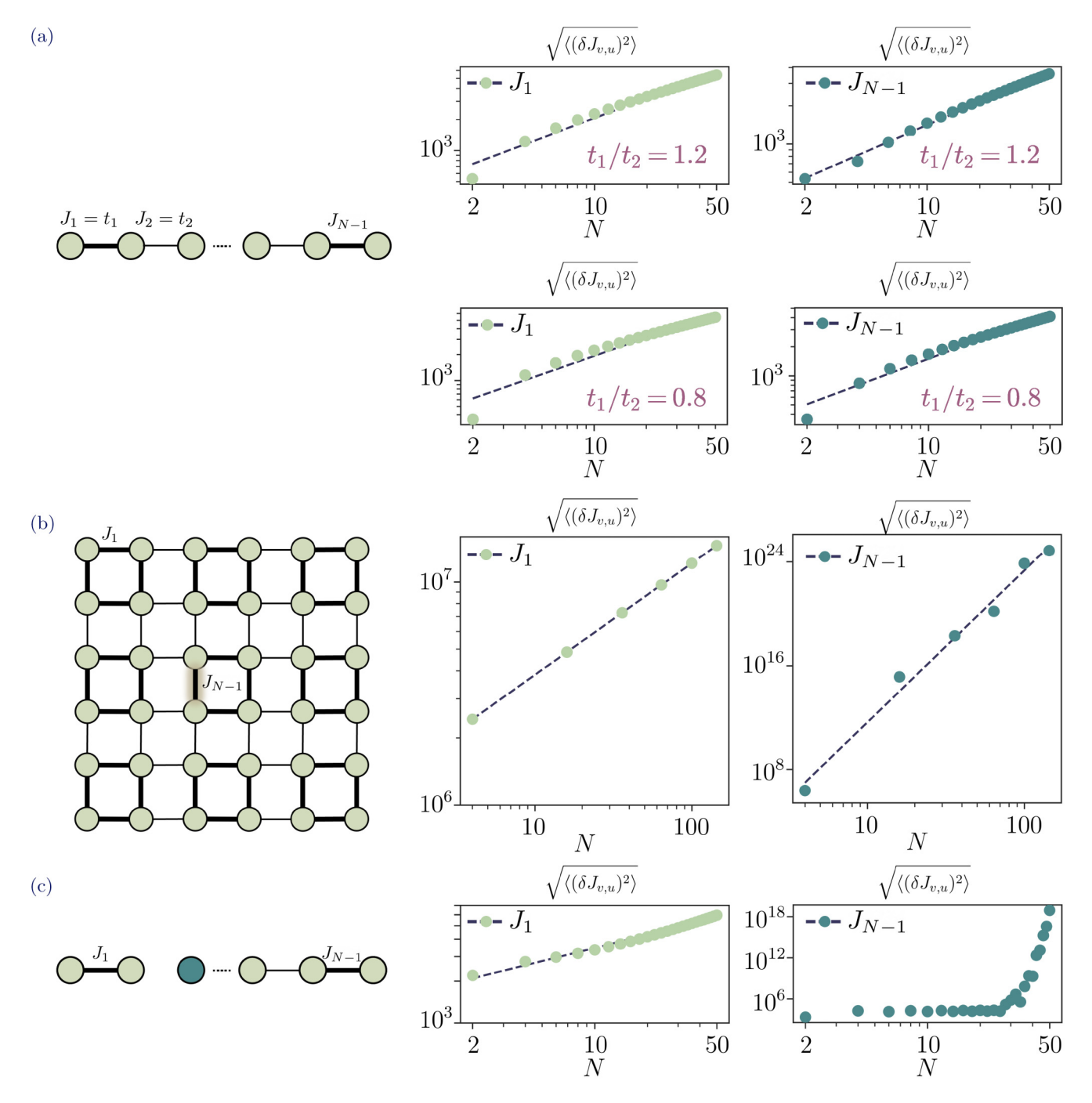


FIG. 7. Stability analysis. The x axis denotes the number of sites in the array on a log scale; y axis denotes the error metric $\sqrt{\langle(\delta J_{v,u})^2\rangle}$ on a log scale. (a) Schematic depicting a 1D SSH. Error metric plot for a SSH chain with $t_1/t_2=1.2$ (without edge states) and $t_1/t_2=0.8$ (with edge states) [42]. (b) Schematic depicting a 2D SSH. Error metric plot for a SSH 2D lattice with $t_1/t_2=1.2$. Each point is in 100 point average with disorder in on-site potentials to be 10 MHz to avoid absolute degeneracies. (c) Schematic depicting a 1D SSH with a defect site at N/2 such that $\mu_{N/2}=\mu_{N/2}+2t_1$. Error metric plot such that $t_1/t_2=1.2$. As evident, error metric for J_{N-1} depicts a breakdown in stability.

obtain that

$$\langle (\delta J_{v,u})^2 \rangle = \sum_{\alpha,v',u'} \left| \frac{\partial J_{v,u}}{\partial M_{\alpha,v',u'}^{(1)}} \right|^2 \text{ and}$$

$$\langle (\delta \chi_v)^2 \rangle = \sum_{v',u'} \left(\sum_{\alpha} \left| \frac{\partial \chi_v}{\partial M_{\alpha,v',u'}^{(1)}} \right|^2 + \sum_{\bar{\alpha}} \left| \frac{\partial \chi_v}{\partial C_{\bar{\alpha},v',u'}^{(2)}} \right|^2 \right).$$

In Fig. 7(a), we take a SSH chain with real coupling strengths and plot the behavior of the defined error metric for the coupling strengths along the first and last edge in the chain. From the plot, we can see that the metric scales polynomially with N. This suggests that even though the amount of errors in the reconstructed coupling strengths increases with N, we only need a polynomial increase in the number of measurements to accurately determine the Hamiltonian in question. We show

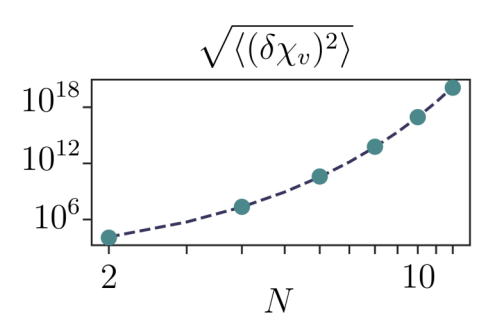


FIG. 8. Stability analysis where x axis (log scale) denotes number of sites in the array and y axis (log scale) denotes the error metric $\sqrt{\langle (\delta \chi_v)^2 \rangle}$ in χ_N for a SSH chain with $J_1/J_2=1.2$. $\sqrt{\langle (\delta \chi_v)^2 \rangle}$ scales polynomially with N on a log scale. We assume $\delta J=0$.

the same for a 2D SSH-like model in Fig. 7(b). We expect this linear scaling of error (on a log scale) for models with delocalized eigenvectors. If, however, we have a localized state, then to accurately determine the Hamiltonian parameters in the interior of the lattice may require exponentially accurate measurements. For example, consider a SSH chain with at least one strongly localized eigenvector obtained by inducing a defect site in the middle such that the on-site potential of this site is greater than two times the maximum coupling in the chain. This localized eigenvector will rapidly decay away from the defect site as we approach the edge site at which measurements can be performed. Hence, we expect that in this case there will exist a N after which a small error in the measurement of coefficients will lead to a blowup in the error of the estimated coupling strengths. We plot this case in Fig. 7(c). We confirm from the plot that after a specific N the error metric scales polynomially, implying that an exponentially large number of measurements will be needed to accurately determine the realized Hamiltonian after this point.

Lastly, we move onto the second stage of the tomography scheme, involving reconstruction of χ s. We again use a similar 1D SSH chain and plot the behavior of $\sqrt{\langle (\delta \chi_v)^2 \rangle}$ in Fig. 8 assuming zero error in reconstruction of couplings as the number of sites N increases. We notice that the error metric scales polynomially with N on a log scale, which implies that reconstructing the nonlinear part of the Hamiltonian requires an exponentially large number of measurements as the number of sites N increases. This indicates that this algorithm despite being applicable for lossy lattices with complex hopping rates is only practical when the size of the photonic lattice (characterized by N) is small. Now, however, if we assume an additional capability in the system under investigation, such that the on-site nonlinearity can be toggled on and off during the experiment at all nodes, there exists a modification of the algorithm that remains stable irrespective of the system size N. The assumption of control over on-site nonlinearity is generally valid for most on-chip typical quantum simulators, as local tunability is a necessity to precisely program the terms of the Hamiltonian being implemented [1]. In these systems, obtaining concurrent local measurability with local control is experimentally challenging due to the difficulty in placing impedance-matched read-out resonators (for superconducting systems) or lossless waveguides (for photonics) in proximity of the densely packed resonator arrays used to realize these bosonic lattices [4,10,12,43,44]. Hence, our modification that overcomes this issue can be useful for tomography of nonlinearities in such bosonic lattices. Under this assumption, the nonlinearity for any site $v \in \mathcal{V}$ can be calculated as

$$\chi_v = \text{Tr}(H) - \text{Tr}(H_{v,\text{off}}) = \sum_{\alpha} \left(E_{\alpha}^{(2)} - E_{\alpha,v,\text{off}}^{(2)} \right),$$

where $E_{\alpha, {\rm off}}^{(2)}$ denotes the eigenenergies in the two-photon subspace of the lattice measured at the boundaries with nonlinearity at site v: χ_v turned off, $H_{v, {\rm off}}$ denotes the corresponding system Hamiltonian.

IV. QUANTUM ENHANCEMENT PROTOCOL

The algorithm described in Sec. III, while in several experimentally relevant settings allows us to stably reconstruct the Hamiltonian parameters, operates at the SQL. More precisely, suppose our goal is to reconstruct the Hamiltonian parameters to a precision ε . Then, the precision required in the boundary measurements (either transmission or two-photon correlation) is also $\varepsilon_{\rm bd} = \Theta(\varepsilon)$. Consequently, even in an ideal setting of no experimental measurement errors, the number of photons (used as independent measurement trials) needed to achieve this target precision scales as $1/\varepsilon_{\rm bd}^2 \sim O(1/\varepsilon^2)$, which is the well-known standard quantum limit. We point out that $\varepsilon_{\rm bd}$ can either scale polynomially with N or exponentially (superpolynomially) with N depending on the spectral properties of the Hamiltonian in question (e.g., see the discussion in Sec. III C). Throughout this section, we will focus on the dependence of $\varepsilon_{\rm bd}$ on the target precision ε and suppress the dependence of $\varepsilon_{\rm bd}$ on N.

A natural question to ask is if the dependence on the number of measurements on ε can be improved to beyond $1/\varepsilon^2$ using techniques from quantum-enhanced sensing. In this section, we address this question, and adapt techniques from quantum-enhanced interferometry to obtain a tomography protocol which assumes (a) boundary excitation and measurement access and (b) ability to toggle the nonlinear term in the Hamiltonian, and beats the standard quantum limit. We point out that, while compared to the tomography method described in Sec. III, we additionally require the ability to switch on and off the nonlinear term in the Hamiltonian for the protocol described in this section. This requirement is satisfied in many experimental systems [4,12,43], and introducing this ability is typically experimentally much easier than being able to excite and measure at a site in the bulk of the lattice [4,10,12,43,44].

A. Reconstructing μ_v and $J_{v,u}$

Consider first determining the single-particle parameters $J_{v,u}$ and μ_v . Here, the number of photons needed to sense these parameters can be quadratically improved by using the standard Fock-state interferometry [32,33]. More precisely, instead of using N single photons to perform the transmission measurement, we can instead use the setup depicted in Fig. 9—boundary sites $v, u \in \mathcal{V}_0$ are coupled to one arm of a Mach-Zender interferometer (MZI) and throughout this measurement, we turn off the nonlinear term in the Hamiltonian.

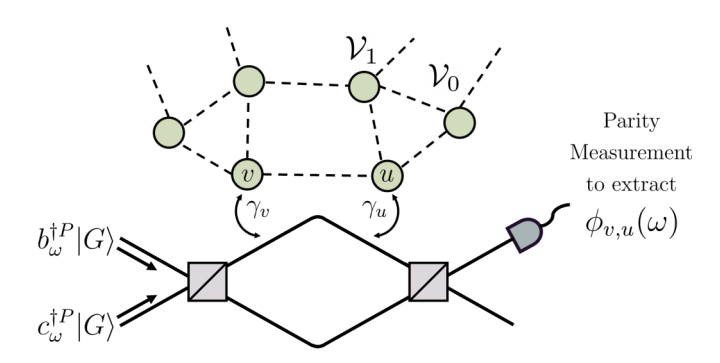


FIG. 9. Obtaining a quantum enhancement in the measurement of the single-particle parameters $J_{v,u}$ and μ_v by using it as the phase-shifting element in the standard Fock state spectroscopy setup

The lattice effectively acts as a (frequency-dependent) phase shifter, with the phase imparted to the MZI arm given by

$$\phi_{v,u}(\omega) = \arg\left(1 + i \sum_{\alpha,u,v} \frac{\sqrt{\gamma_u \gamma_v} M_{\alpha,u,v}^{(1)}}{\omega - E_{\alpha}^{(1)}}\right).$$

Clearly, measuring $\phi_{v,u}(\omega)$ allows us to determine the coefficients $E_{\alpha}^{(1)}$, and $M_{\alpha,u,v}^{(1)}$. A parity measurement on the output port of the MZI allows us to measure the phase imparted to the photons due to scattering from the boundary site v to a precision of $O(P^{-1})$ [32,33], which in turn allows us to determine $M_{\alpha,v,u}^{(1)}$ to a precision $\varepsilon_{\rm bd} = O(P^{-1})$. Applying the algorithm described in Sec. III therefore allows us to determine μ_v and $J_{v,u}$ to precision ε with $O(\varepsilon^{-1})$ photons, thus yielding a quadratic improvement over the standard quantum limit.

B. Reconstructing χ_ν

Obtaining a quantum enhancement in precision of non-linearities χ_{ν} 's is more challenging than simply using the Fock state spectroscopy setup since, in the presence of the on-site nonlinearity, which in turn induces photon-photon interactions, an incident Fock state is scattered into a complex multimode state from which extracting χ_{ν} is not straightforward. Instead, by carefully turning on and off the nonlinearity in the lattice, below we describe a scheme that can still be used to obtain a quantum enhancement.

1. Protocol

Suppose we want to estimate nonlinearity χ_v at a site $v \in \mathcal{V}$ —we adapt the standard NOON state interferometry [34] and couple a boundary site to one of the two ports that are carrying the NOON state [Fig. 10(a)]. First, with the nonlinearity turned off, we excite the boundary sites to initialize the system in a superposition of vacuum and the P photon Fock state at site v, i.e., in the state $|\Psi_{P,v}\rangle$,

$$|\Psi_{P,v}\rangle = \frac{1}{\sqrt{2}} \left(|0\rangle \otimes |P\rangle_{\text{ref}} + e^{i\alpha} \frac{a_v^{\dagger P}}{\sqrt{P!}} |G\rangle \otimes |G\rangle_{\text{ref}} \right), \quad (13)$$

where $|P\rangle_{\rm ref}$ ($|G\rangle_{\rm ref}$) refers to the P-photon (0-photon) state in the reference port not coupled to the lattice, and α is a reference phase that we will pick later. Since the single-particle parameters have already been measured and the nonlinearities

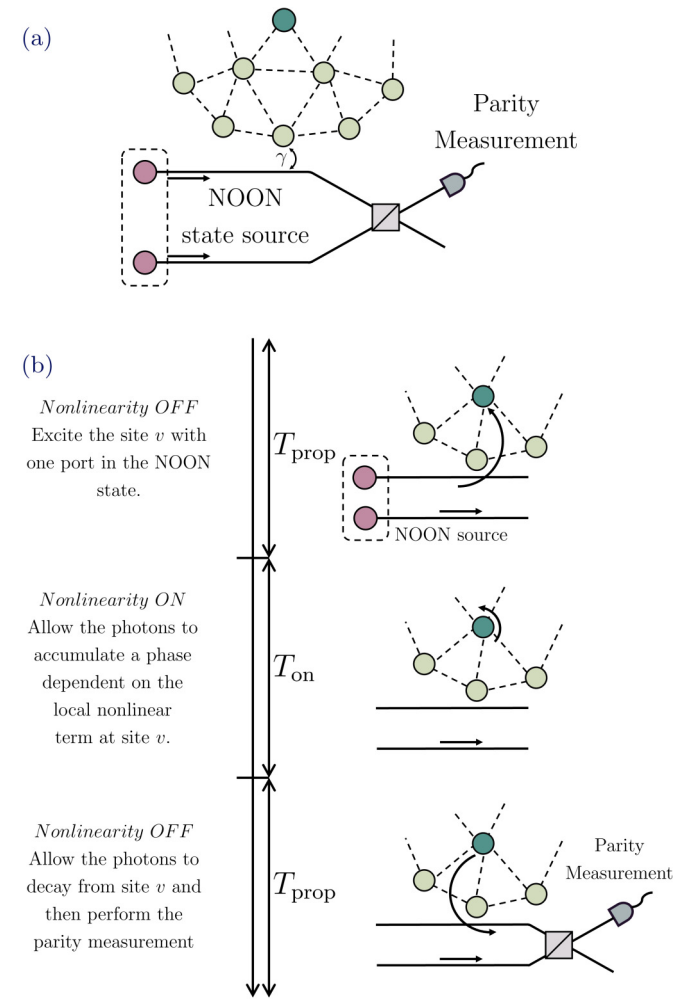


FIG. 10. (a) Setup depicting the use of NOON states in obtaining quantum enhancement in extracting the required Hamiltonian parameters. (b) The proposed parity measurement scheme. $T_{\rm prop}$ denotes the propagation time for photons to reach from the coupling waveguide to the site of interest. The nonlinearity remains off during this interval. $T_{\rm on}$ denotes the interval where the nonlinearity at the site of interest is turned on. This interval is again followed up with a time interval $T_{\rm prop}$ which allows photons to couple back into the input (output) waveguide. The required quantities can then obtained by performing a parity measurement.

are turned off, this can be done entirely with access to the boundary sites. More concretely, we couple the interferometer port to a boundary site [Fig. 10(a)] and then compute the wave packet that is emitted into this port if a single particle is initialized at site v and allowed to evolve with respect to the Hamiltonian H. Then, the P photons in the mode coupling to the lattice are prepared in the time reversed wave packet, and the P photons in the other mode in the interferometer are prepared in the emitted wave packet. This state, when made incident on the lattice, excites P particles at site v and, furthermore, when these P photons are emitted back into the port, they can be interfered without a mode mismatch with the photons in the other port. Appendix B provides explicit details about the computation of this wave packet, as well as

on how a NOON, in a given wave packet, can be prepared experimentally.

However, we need to account for the fact that the single-particle parameters are not known exactly from the first stage of the tomography algorithm and, consequently, this process, instead of preparing the state $|\Psi_{P,v}\rangle$ in Eq. (13), prepares a state $|\hat{\Psi}_{P,v}\rangle$, where

$$|\hat{\Psi}_{P,v}\rangle = \frac{1}{\sqrt{2}}(|G\rangle \otimes |P\rangle_{\text{ref}} + e^{i\alpha}|\hat{\psi}_{P,v}\rangle \otimes |G\rangle_{\text{ref}}),$$
 (14)

where $|\psi_{P,v}\rangle$ approximates the state $a_v^{\dagger P}|G\rangle/\sqrt{P!}$. In particular, we assume that the coefficients $J_{v,u}$ and μ_v are determined to a precision ε_0 , and that the photons decay into the output port, from any site in the interior, in time approximately T_{prop} . Equivalently, for the time-reversed wave packet to excite a photon at the target site, it can be shown that for all $v \in \mathcal{V}$ (see Appendix B for a detailed proof):

$$\left\| \frac{a_{v}^{\dagger P}}{\sqrt{P!}} |G\rangle - |\hat{\psi}_{P,v}\rangle \right\| \leqslant \sqrt{T_{\text{prop}}PN(d+1)\varepsilon_{0}}. \tag{15}$$

Note that increasing the number of photons P used for reconstructing χ_v also increases the error between $a_v^{\dagger P}|G\rangle/\sqrt{P!}$ and $|\hat{\psi}_{P,v}\rangle$. Consequently, the precision ε_0 of the single-particle parameters, as reconstructed from the first stage of this algorithm, would need to be decreased with P, which would imply that the number of photons used in that stage would need to increase with P. However, as we argue below, to obtain even a super Heisenberg scaling in precision of χ_v , the overhead needed in terms of the number of photons from the first stage of the algorithm is much less than P, and thus does not impact the super Heisenberg scaling obtained for χ_v .

Next, we turn on the nonlinearity χ_v at site v for a time period $T_{\rm on}$, which remains to be chosen. If $T_{\rm on}$ is sufficiently short, then the P particles initialized at site v does not diffuse significantly to the neighboring sites, and we prepare a state

$$|\hat{\Phi}_{P,v}\rangle = e^{-iHT_{\text{on}}}|\hat{\Psi}_{P,v}\rangle,\tag{16}$$

which approximates the state $|\Phi_{P,v}\rangle$, where

$$|\Phi_{P,v}\rangle = \frac{1}{\sqrt{2}} \bigg(|G\rangle \otimes |P\rangle_{\text{ref}} + e^{i(\alpha - \theta_{P,v})} \frac{a_v^{\dagger P}}{\sqrt{P!}} \otimes |G\rangle_{\text{ref}} \bigg),$$
(17a)

where

$$\theta_{P,v} = \left(\mu_v P + \frac{\chi_v P(P-1)}{2}\right) T_{\text{on}}.$$
 (17b)

A more careful analysis of this stage, detailed in Appendix B, allows us to provide the following quantitative upper bound on the error between $|\psi\rangle$ and $|\phi_{P_n}\rangle$:

$$\||\hat{\Phi}_{P,v}\rangle - |\Phi_{P,v}\rangle\| \leqslant \sqrt{P}JdT_{\text{on}} + \sqrt{T_{\text{prop}}PN(d+1)\varepsilon_0},$$
 (18)

where d is the degree of the graph $(\mathcal{V},\mathcal{E})$ describing the lattice (i.e., the maximum number of edges incident on any one vertex) and J is an upper bound on the coupling coefficients $J_{v,u}$ (i.e., $|J_{v,u}| \leq J$ for all $(v,u) \in \mathcal{E}$). This upper bound implies that for short enough $T_{\text{on}} \leq O(P^{-1/2})$, then the error between $\||\hat{\Phi}_{P,v}\rangle - |\Phi_{P,v}\rangle\|$ can be controlled to remain small even when increasing P.

Finally, we can now measure the phase $\theta_{P,v}$ introduced in Eq. (17) by performing the parity measurement after applying a beam splitter operation. Choosing $\alpha=0$ and $\pi/2$ in the original NOON state yields an expected outcome of the quadratures $\cos(\theta_{P,v})$ and $\sin(\theta_{P,v})$, respectively. These expectation values then allow us to extract $\theta_{P,v}$ —however, just the probabilistic nature of the measurement yields that there is a constant (i.e., P independent error) in the measured quadratures. However, since $d\chi_v/d\theta_{P,v}=2/P(P-1)T_{\rm on}$, being able to measure $\theta_{P,v}$ to a constant precision allows us to measure χ_v to a precision that is enhanced by a factor of $1/P(P-1)T_{\rm on}$.

2. Sensitivity analysis

In the remainder of this subsection, we sketch the sensitivity analysis of the protocol described above—a rigorous and detailed version of this analysis is provided in Appendix B. In the idealized setting of no experimental errors, there are three sources of errors in our protocol. First is the error in the measured single-particle parameters $J_{v,u}$ and μ_v determined in the first stage of the protocol and used for designing the incident NOON state's wave packet. This manifests as an error between $|\hat{\Psi}_{P,v}\rangle$ and $|\Psi_{P,v}\rangle$ defined in Eqs. (13) and (14), respectively. Second is the error arising due to the diffusion of photons into the sites other than the target site v, which manifests as an error between $|\hat{\Phi}_{P,v}\rangle$ and $|\Phi_{P,v}\rangle$ defined in Eqs. (16) and (17). Finally, there is the measurement error in the outcome of the parity measurement to determine the quadrature $\cos(\theta_{P,v})$ and $\sin(\theta_{P,v})$.

To ensure that the quantum state finally prepared between site v and the reference beam does not deviate significantly from the ideal state $|\Phi_{P,v}\rangle$ defined in Eq. (16) due to the state errors in the first two stages of the protocol estimated in Eqs. (15) and (B11), we choose $\varepsilon_0 \leq O(1/P)$ and $T_{\rm on} \leq O(1/\sqrt{P})$. Note if we use the quantum enhanced twin-Fock state interferometry to determine the single-particle parameters, as described in Sec. IV A, the number of photons required in this stage will be $O(\varepsilon_0^{-1}) = O(P)$, which is only a constant-factor overhead. Assuming that we use O(1) measurements of the parity operator to reduce its error to $\leq O(1)$, and accounting for the other sources of (15) and (B11), $\theta_{v,P}$ can be determined to precision $\delta\theta_{P,v}$ given by

$$\delta\theta_{P,v} \leqslant O(1) + O(\sqrt{P\varepsilon_0}) + O(\sqrt{P}T_{\text{on}}) \leqslant O(1),$$

where we have suppressed the dependence on N and T_{prop} , since they are independent of P. Thus, we can now estimate the error ε in χ_{v} as

$$\varepsilon \sim \frac{\delta \theta_{P,v}}{d\theta_{P,v}/d\gamma_v} \sim O(T_{\rm on}^{-1} P^{-2}) \sim O(P^{-3/2}),$$

which yields the super-Heisenberg scaling of $P = O(\varepsilon^{-2/3})$, improving over the $O(\varepsilon^{-2})$ of the classical tomography protocol for this problem.

V. CONCLUSION

In this paper, we developed an algorithm for tomography of nonlinear topological quantum bosonic lattices with measurement accessibility only to the perimeter of the lattice. We numerically demonstrated the stability of our algorithm and then proposed an extension to the algorithm to quantum mechanically enhance the precision of the estimated Hamiltonian. This algorithm can also likely be extended to include other experimentally relevant quantum simulation setups like spin chains or quantum emitters coupled to such photonic lattices. Furthermore, if next-nearest-neighbor couplings are present, the boundary may not be sufficient to satisfy the graph infection. Therefore, future directions could include tomography of the next-nearest couplings and additional Hamiltonian terms. Additionally, while we only numerically studied the stability of the reconstruction algorithm, making progress in its rigorous mathematical analysis would also help in understanding the practical utility and limitations of this algorithm.

ACKNOWLEDGMENTS

We thank A. Gorshkov for helpful discussions. A.M. acknowledges support from the National Science Foundation Grants No. NSF-QII-TAQS-1936100 and No. NSF-1845009.

APPENDIX A: DETAILS OF THE TOMOGRAPHY ALGORITHM: DETAILED ALGORITHM

1. Extracting $M^{(1)}_{\alpha,v,u}, M^{(2)}_{\vec{\alpha},v,u}$ from transmission and two-photon correlation functions

In this Appendix, we provide details of how the transmission and two-photon correlation functions can be used to obtain the data on $M_{\alpha,v,u}^{(1)}$ and $M_{\tilde{\alpha},v,u}^{(2)}$. Before proceeding further, we note a basic fact about complex functions—suppose $f(\omega)$ is a complex valued function of ω which is of the form

$$f(\omega) = \frac{1}{\sqrt{2\pi}} \sum_{i=1}^{n} \left(\frac{F_j}{i(E_j - \omega) + \Gamma_j/2} \right),$$

where F_j are complex numbers, E_j , Γ_j are real numbers, and $E_j \neq E_k$ for $j \neq k$. Then, it follows from the Filter diagonalization method of Ref. [45] that the function $f(\omega)$, if known for all $\omega \in \mathbb{R}$, uniquely determines F_j , E_j , Γ_j .

In both of the following subsections, we consider the setup shown in Fig. 1: the lattice is coupled to an input port, with time-domain annihilation operator b_{τ} , through the vertex u and to an output port, with time-domain annihilation operator c_{τ} , through the vertex v. The input port is then excited through an incident multitone laser pulse with frequencies $\omega_1, \omega_2 \dots \omega_M$, amplitude B_0 , pulse width τ_w , and pulse shape $\zeta(\tau)$. This can be described by the coherent state

$$|\psi_{\mathrm{in}}\rangle = \exp\left(-\frac{1}{2}\int_{-\infty}^{\infty}|f_{B_0,\tau_w}(\tau)|^2d\tau\right) \ imes \sum_{l=0}^{\infty}\frac{1}{k!}\left(\int_{-\infty}^{\infty}f_{B_0,\tau_w}(\tau)b_{\tau}^{\dagger}d\tau\right)^k|G\rangle,$$

where

$$f_{B_0,\tau_w}(\tau) = B_0 \zeta \left(\frac{\tau}{\tau_w}\right) \left(\sum_{i=1}^M e^{-i\omega_i \tau}\right).$$

For concreteness, we take $\zeta(\tau)$ to be a smooth function that falls off to 0 as $|\tau| \to \infty$ faster than any polynomial in τ (i.e.,

 ξ is a Schwartz function) and fix its normalization by setting $\zeta(0) = 1$. It is convenient to define $|\phi_{\rm in}^{(k)}\rangle$ via

$$|\phi_{
m in}^{(k)}
angle = rac{1}{B_0^k}igg(\int_{-\infty}^\infty f_{B_0, au_w}(au)b_ au^\dagger d auigg)^k|G
angle.$$

We perform a homodyne detection on the output port. The same laser pulse, with possibly a controllable phase φ , is interfered with the output port through a 50-50 beam splitter, and either a transmission or a two-photon correlation function measurement is performed at (one of the) beam-splitter output ports.

To extract information about the single- and two-particle spectra, we will consider the regime of continuous-wave excitation and weak driving. The continuous wave limit would correspond to $\tau_w \to \infty$ and the weak drive limit would correspond to $B_0 \to 0$ —however, pointed out in Ref. [37], the order of these limits is important. For example, taking the limit of $B_0 \to 0$ before $\tau_w \to \infty$ simply results in $|\psi_{\rm in}\rangle$, reducing to the vacuum state $|G\rangle$, while taking the limit of $\tau_w \to \infty$ without taking $B_0 \to 0$ does not exist. The resolution of this issue, as pointed out in Ref. [37], was to consider the transmission and the second-order correlation functions of the scattered photons normalized to B_0^2 and B_0^4 , respectively, then take the weak driving limit $(B_0 \to 0)$ followed by the continuous wave limit $\tau_w \to \infty$.

Below, we execute this procedure for our setup and for first- and second-order correlation functions obtained in a Homodyne detection setup. In particular, we establish that the outcome of this detection allows us to obtain $E_{\alpha}^{(1)}, E_{\alpha}^{(2)}, M_{\alpha,v,u}^{(1)}, M_{\bar{\alpha},v,u}^{(2)}$, where v, u are vertices at the boundary. A subtlety that was implicitly assumed but not rigorously outlined in Ref. [37] is that the effective Hamiltonian within the single- and two-excitation subspaces, $\mathbf{H}_{\mathrm{eff}}^{(1)} \in \mathbb{C}^{|\mathcal{V}| \times |\mathcal{V}|}$ and $\mathbf{H}_{\mathrm{eff}}^{(2)} \in \mathbb{C}^{|\mathcal{V}|(|\mathcal{V}|-1)/2 \times |\mathcal{V}|(|\mathcal{V}|-1)/2}$, have all eigenvalues with negative imaginary parts, i.e., they do not support any bound states. Under this assumption together with assuming that the matrices $\mathbf{H}_{\mathrm{eff}}^{(1)}, \mathbf{H}_{\mathrm{eff}}^{(2)}$ are diagonalizable, we then obtain that

$$\|\exp\left(-i\mathbf{H}_{\text{eff}}^{(k)}t\right)\| \leqslant C_k e^{-\sigma_k t}$$
 (A1)

for some constants C_k , $\sigma_k > 0$. To see this, we can first invoke the diagonalizability of $\mathbf{H}_{\mathrm{eff}}^{(k)}$ to express it as $\mathbf{H}_{\mathrm{eff}}^{(k)} = \mathbf{P}^{(k)} \mathrm{diag}(\boldsymbol{\lambda}^{(k)}) \mathbf{P}^{(k)^{-1}}$. Then, we have that

$$\begin{aligned} \left\| \exp\left(-i\mathbf{H}_{\text{eff}}^{(k)}t\right) \right\| &= \|\mathbf{P}^{(k)} \operatorname{diag}(e^{-i\boldsymbol{\lambda}^{(k)}t})\mathbf{P}^{(k)^{-1}} \| \\ &\leqslant \|\mathbf{P}^{(k)}\| \|\mathbf{P}^{(k)^{-1}}\| \|\exp(-i\boldsymbol{\lambda}^{(k)}t)\|. \end{aligned}$$

Noting that $\|\exp(-i\lambda^{(k)}t)\| \le e^{-\sigma_k t}$, where σ_k is the smallest magnitude imaginary part of the eigenvalues $\lambda^{(k)}$, and setting $C_k = \|\mathbf{P}^{(k)}\| \|\mathbf{P}^{(k)^{-1}}\|$, we obtain the bound in Eq. (A1).

a. Analyzing the homodyned transmission measurement

We first consider performing a transmission measurement at the output port following the beam splitter, while using only one laser frequency ω_L [i.e., $f_{B_0,\tau_w}(\tau) = B_0\zeta(\tau/\tau_w)e^{-i\omega_L\tau}$]. The incident photon flux at position τ in the input port is given by $\langle \psi_{\rm in}|b_\tau^\dagger b_\tau|\psi_{\rm in}\rangle = B_0^2|\zeta(\tau/\tau_w)|^2 \to B_0^2$ as $\tau_w \to \infty$. The transmission in the output waveguide in the weak-driving limit, on accounting for the homodyne measurement and

normalizing to the input photon flux, is given by

$$\begin{split} T(\omega_L) &= \lim_{\tau_w \to \infty} \lim_{B_0 \to 0} \frac{1}{2B_0^2} \langle \psi_{\rm in} | \hat{\mathbf{S}}^\dagger (c_\tau^\dagger + e^{-i\varphi} f_{B_0,\tau_w}^*(\tau)) \\ &\times (c_\tau + e^{i\varphi} f_{B_0,\tau_w}(\tau)) \hat{\mathbf{S}} | \psi_{\rm in} \rangle, \\ &= \lim_{\tau_w \to \infty} \frac{1}{2} \left| \langle G | c_\tau \hat{\mathbf{S}} | \phi_{\rm in}^{(1)} \rangle + \zeta \left(\frac{\tau}{\tau_w} \right) e^{i(\varphi - \omega_L \tau)} \right|^2, \\ &= \frac{1}{2} \left| \lim_{\tau_w \to \infty} \langle G | c_\tau \hat{\mathbf{S}} | \phi_{\rm in}^{(1)} \rangle + e^{i(\varphi - \omega_L \tau)} \right|^2, \end{split}$$

where τ is any time point. As we will see below, in the continuous-wave limit, any dependence on τ of the transmission will vanish. An expression for $\langle G|c_{\tau}\hat{S}|\phi_{\rm in}^{(1)}\rangle$ can be obtained from standard scattering theory [35,36] to obtain

$$\langle G|c_{\tau}\hat{\mathbf{S}}|\phi_{\mathrm{in}}^{(1)}\rangle = -\sqrt{\gamma_{c}\gamma_{b}} \int_{-\infty}^{\infty} \langle G|\mathcal{T}[\tilde{a}_{v}(\tau)\tilde{a}_{u}^{\dagger}(s)]|G\rangle\zeta$$
$$\times \left(\frac{s}{\tau_{w}}\right) e^{-i\omega_{L}s} ds, \tag{A2}$$

where $\tilde{a}_v(s) = e^{i\tilde{H}_{\rm eff}s}a_ve^{-i\tilde{H}_{\rm eff}s}$, where $\tilde{H}_{\rm eff}$ also includes non-Hermitian terms arising due to the coupling of a_v , a_u with the input and output ports, i.e., $\tilde{H}_{\rm eff} = H_{\rm eff} - i(\gamma_b a_u^\dagger a_u + \gamma_c a_v^\dagger a_v)/2$, where $H_{\rm eff}$ is defined in Eq. (1). We now take the continuous-wave limit of $\tau_w \to \infty$. This requires us to swap

the order of the limit and integral in Eq. (A2). The legitimacy of this swap follows from the dominated convergence theorem. To see this, we first note that

$$\langle G|\mathcal{T}[\tilde{a}_v(\tau)\tilde{a}_u^{\dagger}(s)]|G\rangle$$

$$= \begin{cases} \mathbf{e}_v^{\mathsf{T}} \exp\left(-i\mathbf{H}_{\mathrm{eff}}^{(1)}(\tau - s)\right)\mathbf{e}_u & \text{if } s \leqslant \tau \\ 0 & \text{otherwise,} \end{cases}$$

where $\mathbf{e}_v \in \mathbb{C}^{|\mathcal{V}|}$ is a unit vector with a 1 at the location of the vertex v. Furthermore, it follows from Eq. (A1) that for all $\tau_w > 0$ and $s \leqslant \tau$,

$$\begin{aligned} \left| \mathbf{e}_{v}^{\mathrm{T}} \exp \left(-i \mathbf{H}_{\mathrm{eff}}^{(1)}(\tau - s) \right) \mathbf{e}_{u} \zeta \left(\frac{s}{\tau_{w}} \right) e^{-i\omega_{L} s} \right| \\ & \leq \left\| \exp \left(-i \mathbf{H}_{\mathrm{eff}}^{(1)}(\tau - s) \right) \right| \left| \zeta \left(\frac{s}{\tau_{w}} \right) \right| \\ & \leq C_{1} e^{-\sigma_{1}(\tau - s)} \|\zeta\|_{\infty}, \end{aligned}$$

where $\|\zeta\|_{\infty} = \sup_{t \in \mathbb{R}} |\zeta(t)|$. Thus, for all $\tau_w > 0$, the integrand in Eq. (A2) is upper bounded by the function $g(s) = C_1 e^{-\sigma_1(\tau - s)} \|\zeta\|_{\infty}$ if $s \leq \tau$ and 0 if $s > \tau$, which is also absolutely integrable. Thus, the integral in Eq. (A2) satisfies the conditions of the dominated convergence theorem, and consequently,

$$\begin{split} \lim_{\tau_w \to \infty} \int_{-\infty}^{\infty} \langle G | \mathcal{T}[\tilde{a}_v(\tau) \tilde{a}_u^{\dagger}(s)] | G \rangle \zeta \left(\frac{s}{\tau_w} \right) e^{-i\omega_L s} ds &= \int_{-\infty}^{\infty} \left(\lim_{\tau_w \to \infty} \langle G | \mathcal{T}[\tilde{a}_v(\tau) \tilde{a}_u^{\dagger}(s)] | G \rangle \zeta \left(\frac{s}{\tau_w} \right) e^{-i\omega_L s} \right) ds, \\ &= \int_{-\infty}^{\infty} \langle G | \mathcal{T}[\tilde{a}_v(\tau) \tilde{a}_u^{\dagger}(s)] | G \rangle e^{-i\omega_L s} ds. \end{split}$$

Evaluating this integral, we then obtain that

$$\lim_{\tau_w \to \infty} \langle G | c_{\tau} \hat{\mathbf{S}} | \phi_{\text{in}}^{(1)} \rangle = e^{-i\omega_L \tau} \tau(\omega_L), \quad \text{where } \tau(\omega_L) = i \sqrt{\gamma_c \gamma_b} \mathbf{e}_v^{\text{T}} \big(\tilde{\mathbf{H}}_{\text{eff}}^{(1)} - \omega_L \mathbf{I} \big)^{-1} \mathbf{e}_u = i \sqrt{\gamma_c \gamma_b} \sum_{\alpha} \frac{M_{\alpha, v, u}^{(1)}}{E_{\alpha}^{(1)} - \omega}. \tag{A3}$$

The transmission $T(\omega_L)$, in the continuous-wave limit, can now be expressed as

$$T(\omega_L) = \frac{1}{2} |e^{i\varphi} + \tau(\omega_L)|^2.$$

By varying the phase φ in the homodyning scheme, we can find $\tau(\omega)$ as a function of ω , which then allows us to extract the single-excitation eigenenergies $E_{\alpha}^{(1)}$ and the coefficients $M_{\alpha,v,u}^{(1)}$ for $v,u\in\mathcal{V}_0$, using the filter diagonalization method.

b. Analyzing the homodyned equal-time two-particle correlation function

Two-photon correlation function. Next, we consider the two-particle correlation function, $G^{(2)}(\tau_1, \tau_2; \omega_1, \omega_2)$, measured at the output port on driving the input port with a laser with two tones at ω_1 and ω_2 . In the weak drive limit, we can then express $G^{(2)}(\tau_1, \tau_2; \omega_1, \omega_2)$ as

$$G^{(2)}(\tau_{1}, \tau_{2}; \omega_{1}, \omega_{2}) = \lim_{\tau_{w} \to \infty} \lim_{B_{0} \to 0} \frac{1}{4B_{0}^{4}} \langle \psi_{\text{in}} | \hat{\mathbf{S}}^{\dagger} \prod_{i \in \{1,2\}} (c_{\tau_{i}}^{\dagger} + e^{-i\varphi} f_{B_{0}, \tau_{w}}^{*}(\tau_{i})) \prod_{i \in \{1,2\}} (c_{\tau_{i}} + e^{i\varphi} f_{B_{0}, \tau_{w}}(\tau_{i}))^{2} \hat{\mathbf{S}} | \psi_{\text{in}} \rangle$$

$$= \lim_{\tau_{w} \to \infty} \frac{1}{4} \left| \frac{1}{2} \langle G | c_{\tau_{1}} c_{\tau_{2}} \hat{\mathbf{S}} | \phi_{\text{in}}^{(2)} \rangle + \sum_{i \in \{1,2\}} \frac{e^{i\varphi}}{B_{0}} f_{B_{0}, \tau_{w}}(\tau_{i}) \langle G | c_{\tau_{i}} \hat{\mathbf{S}} | \phi_{\text{in}}^{(1)} \rangle + \frac{e^{2i\varphi}}{B_{0}^{2}} f_{B_{0}, \tau_{w}}(\tau_{1}) f_{B_{0}, \tau_{w}}(\tau_{2}) \right|^{2}$$

$$= \frac{1}{4} \left| |\mathcal{G}^{(c)}(\tau_{1}, \tau_{2}; \omega_{1}, \omega_{2}) + \prod_{i \in \{1,2\}} \left(\sum_{j \in \{1,2\}} (\tau(\omega_{j}) + e^{i\varphi}) e^{-i\omega_{j}\tau_{i}} \right) \right|^{2}, \tag{A4}$$

where, in the summation, $i^c = 1$ if i = 2 and $i^c = 2$ if i = 1 and

$$\mathcal{G}^{(c)}(\tau_1, \tau_2; \omega_1, \omega_2) = \frac{1}{2} \langle G | c_{\tau_1} c_{\tau_2} \hat{\mathbf{S}} | \phi_{\text{in}}^{(2)} \rangle - \langle G | c_{\tau_1} \hat{\mathbf{S}} | \phi_{\text{in}}^{(1)} \rangle \langle G | c_{\tau_2} \hat{\mathbf{S}} | \phi_{\text{in}}^{(1)} \rangle.$$

We now focus on computing the term $\langle G|c_{\tau_1}c_{\tau_2}\hat{S}|\phi_{\rm in}^{(2)}\rangle$. Without loss of generality, we assume that $\tau_1 \geqslant \tau_2$, since $G^{(2)}(\tau_1, \tau_2; \omega_L)$ is invariant under a swap of the two time indices τ_1 , τ_2 . Using the explicit expression for $|\phi_{\rm in}^{(2)}\rangle$, we obtain from standard scattering theory [36,37] that

$$\langle G|c_{\tau_1}c_{\tau_2}\hat{S}|\phi_{\rm in}^{(2)}\rangle = \gamma_c\gamma_b \int_{-\infty}^{\infty} \int_{\infty}^{\infty} \langle G|\mathcal{T}[\tilde{a}_v(\tau_1)\tilde{a}_v(\tau_2)\tilde{a}_u^{\dagger}(s_1)\tilde{a}_u^{\dagger}(s_2)]|G\rangle \Omega_{\omega_1,\omega_2}(s_1,s_2)\zeta\left(\frac{s_1}{\tau_w}\right)\zeta\left(\frac{s_2}{\tau_w}\right)ds_1ds_2,\tag{A5}$$

where $\Omega_{\omega_1,\omega_2}(s_1,s_2)=(e^{-i\omega_1s_1}+e^{-i\omega_2s_1})(e^{-i\omega_1s_2}+e^{-i\omega_2s_2})$. Next, we take the continuous-wave limit $(\tau_w\to\infty)$. Following our previous calculation, we would like to swap the order of this limit and the integral with respect to s_1,s_2 . To justify this swap, we use the dominated convergence theorem for which we need an upper bound on the magnitude of $f(s_1,s_2)=\langle G|\mathcal{T}[\tilde{a}_v(\tau_1)\tilde{a}_v(\tau_2)\tilde{a}_u^\dagger(s_1)\tilde{a}_u^\dagger(s_2)]|G\rangle\Omega_{\omega_1,\omega_2}(s_1,s_2)$. We begin by first noting that $f(s_1,s_2)=f(s_2,s_1)$, so we can assume $s_1\geqslant s_2$ and rewrite

$$\langle G|c_{\tau_1}c_{\tau_2}\hat{\mathbf{S}}\big|\phi_{\mathrm{in}}^{(2)}\big\rangle = 2\gamma_c\gamma_b\int_{-\infty}^{\infty}\int_{-\infty}^{s_1}\langle G|\mathcal{T}[\tilde{a}_v(\tau_1)\tilde{a}_v(\tau_2)\tilde{a}_u^{\dagger}(s_1)\tilde{a}_u^{\dagger}(s_2)]|G\rangle\Omega_{\omega_1,\omega_2}(s_1,s_2)\zeta\left(\frac{s_1}{\tau_w}\right)\zeta\left(\frac{s_2}{\tau_w}\right)ds_2ds_1.$$

Now, for $s_1 \geqslant s_2$,

$$\langle G|\mathcal{T}[\tilde{a}_{v}(\tau_{1})\tilde{a}_{v}(\tau_{2})\tilde{a}_{u}^{\dagger}(s_{1})\tilde{a}_{u}^{\dagger}(s_{2})]|G\rangle = \begin{cases} \mathbf{e}_{v}^{\mathsf{T}}e^{-i\mathbf{H}_{\mathrm{eff}}^{(1)}(\tau_{1}-\tau_{2})}\mathbf{A}_{v}^{(2)}e^{-i\mathbf{H}_{\mathrm{eff}}^{(2)}(\tau_{2}-s_{1})}\mathbf{A}_{v}^{(2)^{\dagger}}e^{-i\mathbf{H}_{\mathrm{eff}}^{(1)}(s_{1}-s_{2})}\mathbf{e}_{u} & \text{if } s_{2} \leqslant s_{1} \leqslant \tau_{2} \leqslant \tau_{1} \\ \mathbf{e}_{v}^{\mathsf{T}}e^{-i\mathbf{H}_{\mathrm{eff}}^{(1)}(\tau_{1}-s_{1})}\mathbf{e}_{u}\mathbf{e}_{v}^{\mathsf{T}}e^{-i\mathbf{H}_{\mathrm{eff}}^{(2)}(\tau_{2}-s_{2})}\mathbf{e}_{u} & \text{if } s_{2} \leqslant \tau_{2} \leqslant s_{1} \leqslant \tau_{1} \\ \mathbf{0} & \text{otherwise,} \end{cases}$$

where $\mathbf{A}_{v}^{(i)}$ is the matrix corresponding to the operator a_{v} when applied to the *i*th excitation subspace. Consequently, we now have that for all $\tau_{w} \geqslant 0$,

$$\left| \langle G | \mathcal{T} [\tilde{a}_v(\tau) \tilde{a}_v(\tau) \tilde{a}_u^{\dagger}(s_1) \tilde{a}_u^{\dagger}(s_2)] | G \rangle \Omega_{\omega_1,\omega_2}(s_1,s_2) \zeta \left(\frac{s_1}{\tau_w} \right) \zeta \left(\frac{s_2}{\tau_w} \right) \right| \leqslant g(s_1,s_2),$$

where

$$g(s_1, s_2) = \begin{cases} 2\|\zeta\|_{\infty}^2 \|\mathbf{A}_{v}^{(2)}\|^2 C_1 C_2 e^{-\sigma_2(\tau - s_1)} e^{-\sigma_1(s_1 - s_2)} & \text{if } s_2 \leqslant s_1 \leqslant \tau_2 \leqslant \tau_1 \\ 2\|\zeta\|_{\infty}^2 C_1^2 e^{-\sigma_1(\tau_1 - s_1)} e^{-\sigma_1(\tau_2 - s_2)} & \text{if } s_2 \leqslant \tau_2 \leqslant s_1 \leqslant \tau_1 \\ 0 & , \end{cases}$$

and it can easily be checked that $g(s_1, s_2)$ is absolutely integrable. Consequently, from the dominated convergence theorem, we obtain that

$$\begin{split} &\lim_{\tau_w \to \infty} \int_{-\infty}^{\infty} \int_{-\infty}^{s_1} \langle G | \mathcal{T}[\tilde{a}_v(\tau_1) \tilde{a}_v(\tau_2) \tilde{a}_u^{\dagger}(s_1) \tilde{a}_u^{\dagger}(s_2)] | G \rangle \Omega_{\omega_1, \omega_2}(s_1, s_2) \zeta \left(\frac{s_1}{\tau_w}\right) \zeta \left(\frac{s_2}{\tau_w}\right) ds_2 ds_1 \\ &= \int_{-\infty}^{\infty} \int_{-\infty}^{s_1} \lim_{\tau_w \to \infty} \langle G | \mathcal{T}[\tilde{a}_v(\tau_1) \tilde{a}_v(\tau_2) \tilde{a}_u^{\dagger}(s_1) \tilde{a}_u^{\dagger}(s_2)] | G \rangle \Omega_{\omega_1, \omega_2}(s_1, s_2) \zeta \left(\frac{s_1}{\tau_w}\right) \zeta \left(\frac{s_2}{\tau_w}\right) ds_2 ds_1 \\ &= \int_{-\infty}^{\infty} \int_{-\infty}^{s_1} \langle G | \mathcal{T}[\tilde{a}_v(\tau_1) \tilde{a}_v(\tau_2) \tilde{a}_u^{\dagger}(s_1) \tilde{a}_u^{\dagger}(s_2)] | G \rangle \Omega_{\omega_1, \omega_2}(s_1, s_2) ds_1 ds_2. \end{split}$$

Now, we can explicitly evaluate this integral by considering different time orderings in the integrand. In particular, we have that

$$\int_{-\infty}^{\infty} \int_{-\infty}^{s_1} \langle G | \mathcal{T}[\tilde{a}_v(\tau_1)\tilde{a}_v(\tau_2)\tilde{a}_u^{\dagger}(s_1)\tilde{a}_u^{\dagger}(s_2)] e^{-i(\omega_1 s_1 + \omega_2 s_2)} ds_1 ds_2 = I_1(\tau_1, \tau_2; \omega_1, \omega_2) + I_2(\tau_1, \tau_2; \omega_1, \omega_2),$$

where

$$I_{1}(\tau_{1}, \tau_{2}; \omega_{1}, \omega_{2}) = \int_{s_{1}=\tau_{2}}^{\tau_{1}} \int_{s_{2}=-\infty}^{\tau_{2}} e^{-i(\omega_{1}s_{1}+\omega_{2}s_{2})} \langle G|a_{v}e^{-iH_{\text{eff}}(\tau_{1}-s_{1})}a_{u}^{\dagger}|G\rangle \langle G|a_{v}e^{-iH_{\text{eff}}(\tau_{2}-s_{2})}a_{u}^{\dagger}|G\rangle ds_{1}ds_{2},$$

$$= -\sum_{k_{1},k_{2}} \frac{\langle G|a_{v}|r_{k_{2}}^{(1)}\rangle \langle l_{k_{2}}^{(1)}|a_{u}^{\dagger}|G\rangle}{(E_{k_{1}}^{(1)}-\omega_{1})} \frac{\langle G|a_{v}|r_{k_{1}}^{(1)}\rangle \langle l_{k_{1}}^{(1)}|a_{u}^{\dagger}|G\rangle}{(E_{k_{2}}^{(1)}-\omega_{2})} (1 - e^{-i(E_{k_{1}}^{(1)}-\omega_{1})(\tau_{1}-\tau_{2})})e^{-i(\omega_{1}\tau_{1}+\omega_{2}\tau_{2})}, \tag{A6}$$

$$I_{2}(\tau_{1},\tau_{2};\omega_{1},\omega_{2}) = \int_{s_{1}=-\infty}^{\tau_{2}} \int_{s_{2}=-\infty}^{s_{1}} e^{-i(\omega_{1}s_{1}+\omega_{2}s_{2})} \langle G|a_{v}e^{-iH_{\text{eff}}(\tau_{1}-\tau_{2})}a_{v}e^{-iH_{\text{eff}}(\tau_{2}-s_{1})}a_{u}^{\dagger}e^{-iH_{\text{eff}}(s_{1}-s_{2})}a_{u}^{\dagger}|G\rangle dt_{1}dt_{2},$$

$$= -\sum_{k_{1},k_{2},k_{3}} \frac{\langle G|a_{v}|r_{k_{1}}^{(1)}\rangle \langle l_{k_{1}}^{(1)}|a_{v}|r_{k_{2}}^{(2)}\rangle \langle l_{k_{2}}^{(2)}|a_{u}^{\dagger}|r_{k_{3}}^{(1)}\rangle \langle l_{k_{3}}^{(1)}|a_{u}^{\dagger}|G\rangle e^{-i(E_{k_{1}}^{(1)}-\omega_{1})(\tau_{1}-\tau_{2})}e^{-i(\omega_{1}\tau_{1}+\omega_{2}\tau_{2})}. \tag{A7}$$

Therefore, we finally obtain that

$$\mathcal{G}^{(c)}(\tau_{1}, \tau_{2}; \omega_{1}, \omega_{2}) = \gamma_{c} \gamma_{b} \sum_{i,j} e^{-i(\omega_{i} + \omega_{j})\tau_{2}} \left(\sum_{\alpha_{1}, \alpha_{2}} \frac{M_{\alpha_{1}, \nu, u}^{(1)} M_{\alpha_{2}, \nu, u}^{(1)} e^{-iE_{\alpha_{1}}^{(1)}(\tau_{1} - \tau_{2})}}{\left(E_{\alpha_{1}}^{(1)} - \omega_{i}\right) \left(E_{\alpha_{2}}^{(1)} - \omega_{j}\right)} - \sum_{\alpha_{1}, \alpha_{2}, \alpha_{3}} \frac{M_{(\alpha_{1}, \alpha_{2}, \alpha_{3}), \nu, u}^{(2)} e^{-iE_{\alpha_{1}}^{(1)}(\tau_{1} - \tau_{2})}}{\left(E_{\alpha_{3}}^{(2)} - \omega_{i} - \omega_{j}\right) \left(E_{\alpha_{3}}^{(1)} - \omega_{j}\right)} \right). \quad (A8)$$

Using Eqs. (A4) and (A8), we can then obtain the following compact expression for $G^{(2)}(\tau_1, \tau_2; \omega_1, \omega_2)$:

$$G^{(2)}(\tau_{1}, \tau_{2}; \omega_{1}, \omega_{2})$$

$$= \left| e^{-i\Delta\tau_{2}} \left(\frac{1}{2} T^{(2)}(\tau; \omega_{1}, \omega_{1}) + e^{-i\omega_{1}\tau} (\tau(\omega_{1}) + e^{i\varphi})^{2} \right) \right.$$

$$+ e^{i\Delta\tau_{2}} \left(\frac{1}{2} T^{(2)}(\tau; \omega_{2}, \omega_{2}) + e^{-i\omega_{2}\tau} (\tau(\omega_{2}) + e^{i\varphi})^{2} \right)$$

$$+ (T^{(2)}(\tau; \omega_{1}, \omega_{2}) + (e^{-i\omega_{1}\tau} + e^{-i\omega_{2}\tau})(\tau(\omega_{1})$$

$$+ e^{i\varphi})(\tau(\omega_{2}) + e^{i\varphi})) \right|^{2}. \tag{A9a}$$

Here $\Delta = \omega_1 - \omega_2$, $\tau = \tau_1 - \tau_2$ and

$$T^{(2)}(\tau;\omega_{1},\omega_{2}) = \sum_{i \in \{1,2\}} \sum_{\alpha_{1},\alpha_{2}} \frac{M_{\alpha_{1},v,u}^{(1)} M_{\alpha_{2},v,u}^{(1)} e^{-iE_{\alpha_{1}}^{(1)}\tau}}{(E_{\alpha_{1}}^{(1)} - \omega_{i})(E_{\alpha_{2}}^{(1)} - \omega_{i})} - \sum_{\alpha_{1},\alpha_{2},\alpha_{3}} \frac{M_{(\alpha_{1},\alpha_{2},\alpha_{3}),v,u}^{(2)} e^{-iE_{\alpha_{1}}^{(1)}\tau}}{(E_{\alpha_{2}}^{(2)} - \omega_{i} - \omega_{i^{c}})(E_{\alpha_{3}}^{(1)} - \omega_{i})},$$
(A9b)

where, again, $i^c=1$ if i=2 and 2 if i=1. $Extracting\ M_{\vec{\alpha},v,u}^{(2)}, E_{\alpha}^{(2)}$. Next, we show how a measurement of $G^{(2)}(\tau_1, \tau_2; \omega_1, \omega_2)$ as a function of $\tau_1, \tau_2, \omega_1, \omega_2$ can be used to determine $M^{(2)}_{\vec{\alpha}, \nu, u}$ and $E^{(2)}_{\alpha}$. Our strategy would be to show that we can extract $T^{(2)}(\tau;\omega_1,\omega_2)$ as a function of τ, ω_1, ω_2 , which can then be used to obtain both $M_{\vec{\alpha}, v, u}^{(2)}$ and $E_{\alpha}^{(2)}$. First, we fix $\tau = \tau_1 - \tau_2$, ω_1 , ω_2 , with $\omega_1 \neq \omega_2$, and vary τ_2 . If $\Delta = \omega_1 - \omega_2 \neq 0$, then $G^{(2)}(\tau_1, \tau_2; \omega_1, \omega_2)$, as a function of τ_2 , will be of the form $f(\tau_2) = |C_0 + C_1 e^{-i\Delta \tau_2} +$ $C_{-1}e^{i\Delta\tau_2}|^2$, where $C_0, C_1, C_2 \in \mathbb{C}$. From this function, we can determine $|C_0|$. To see this, note that

$$f(\tau_2) = |C_0|^2 + |C_1|^2 + |C_2|^2 + 2\operatorname{Re}((C_0C_1^* + C_{-1}C_0^*)e^{i\Delta\tau_2}) + 2\operatorname{Re}(C_{-1}C_1^*e^{2i\Delta\tau_2}).$$

This allows for the determination of $A_0 = |C_0|^2 + |C_1|^2 +$ $|C_{-1}|^2$, $A_1 = C_0 C_1^* + C_{-1} C_0^*$, and $A_2 = C_{-1} C_1^*$. From the coefficients A_0, A_1, A_2 , we can then obtain $|C_0|$ by solving $|A_1|^2 + |A_1^2 - 4|C_0|^2 A_2^*| = 2|C_0|^2 (A_0 - |C_0|^2)$. Therefore, we can obtain $|T^{(2)}(\tau; \omega_1, \omega_2) + (e^{-i\omega_1\tau} + e^{-i\omega_2\tau})(\tau(\omega_1) +$ $e^{i\varphi}$) $(\tau(\omega_2) + e^{i\varphi})$ |². We can assume that $\tau(\omega)$ has already been determined by the homodyned transmission measurement. Consequently, by varying φ , we can now determine $T^{(2)}(\tau;\omega_1,\omega_2)$. Since $M^{(1)}_{\alpha,\nu,u}$ and $E^{(1)}_{\alpha}$ are already known, this measurement allows us to determine

$$\sum_{\vec{\alpha}} \frac{M_{\vec{\alpha},v,u}^{(2)} e^{-iE_{\alpha_1}^{(1)}\tau}}{(E_{\alpha_2}^{(2)} - \omega_1 - \omega_2)(E_{\alpha_1}^{(1)} - \omega_1)},$$

as a function of τ , ω_1 and ω_2 , from which both $E_{\alpha}^{(2)}$ and $M_{\vec{\alpha},v,u}^{(2)}$ can be extracted.

APPENDIX B: QUANTUM ENHANCED TOMOGRAPHY

1. Relationship between $\phi_{v,u}$ and $M_{\alpha,v,u}^{(1)}$

Here, we consider the twin Fock-state MZI setup for measuring $\phi_{v,u}$ (Fig. 9). Note that the nonlinearity is switched off for this phase. We consider the lattice coupled to an output port through the sites $w_1, w_2, \dots, w_m \in \mathcal{V}_0$ (Fig. 11). The Hamiltonian of the system and the port in the interaction picture, relative to the Hamiltonian of the port, can be represented as

$$H(t) = H_s + \left(\sum_{i=1}^m g_i a_{w_i} b_{t+\tau_i}^{\dagger} + \text{H.c.}\right),$$

where

$$H_s = \sum_{u,v=1}^N J_{u,v} a_u^{\dagger} a_v,$$

where g_i is the coupling rate of site w_i to the port and, to simplify notation, we have assumed $J_{u,u} = \omega_u$. Here, a_u is the annihilation operator of the bosonic mode at site u, and b_t is the time-domain annihilation operator corresponding to the coupling port. Furthermore, τ_i specifies the position of the port to which site w_i is coupled and m is the total number of

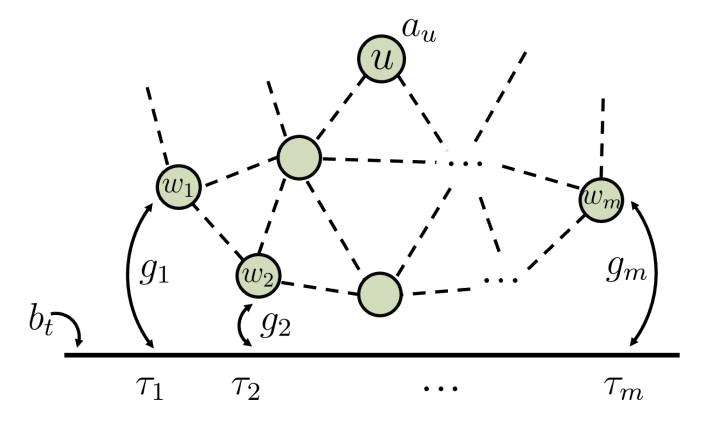


FIG. 11. A schematic representation of the lattice, illustrating its coupling to the port through distinct sites denoted as $w_1, w_2, \ldots, w_m \in \mathcal{V}_0$. Each site w_i is associated with a specific position along the port, characterized by the parameter τ_i . The initial wave function within the port experiences scattering, driven by the Hamiltonian of both the port and lattice. When the nonlinearity is disabled, the output wave packet acquires a phase that depends on its frequency.

sites coupled to the port. Writing the equations of motion for $b_{\tau}(t)$ and $a_{u}(t)$:

$$i\frac{db_{\tau}(t)}{dt} = \sum_{i=1}^{m} a_{w_i}(t)\delta(t+\tau_i-\tau)g_i,$$
 (B1a)

$$i\frac{da_{w_i}(t)}{dt} = \sum_{u} J_{w_i,u} a_u(t) + b_{t+\tau_i}(t) g_i^* \text{ for } i \in \{1, 2, \dots, m\},$$

(B1b)

$$i\frac{da_v(t)}{dt} = \sum_{u} J_{v,u} a_u(t) \text{ otherwise.}$$
 (B1c)

Integrating the first equation,

$$b_{\tau}(t) = b_{\tau}(t_{-}) - i \sum_{i=1}^{m} g_{i} \int_{t_{-}}^{t} a_{w_{i}}(t') \delta(t' + \tau_{i} - \tau) dt'$$

$$= b_{\tau}(t_{-}) - i \sum_{i=1}^{m} g_{i} a_{w_{i}}(\tau - \tau_{i}) \Theta(t_{-} \leqslant \tau - \tau_{i} \leqslant t),$$

where

$$\Theta(a \leqslant t \leqslant b) = \begin{cases} \frac{1}{2} & \text{if} \quad t \in \{a, b\} \\ 1 & \text{if} \quad t \in (a, b) \\ 0 & \text{otherwise.} \end{cases}$$

In particular,

$$b_{t+\tau_j}(t) = b_{t+\tau_j}(t_-) - i \sum_{i=1}^m g_i a_{w_i}(t+\tau_j-\tau_i)\Theta$$

$$\times (t_{-} \leqslant t + \tau_{i} - \tau_{i} \leqslant t).$$

Assuming $\tau_1 < \tau_2 < \cdots < \tau_m$, we have that

$$b_{t+\tau_j}(t) = b_{t+\tau_j}(t_-) - i\frac{g_j}{2}a_{w_j}(t) - i\sum_{i=i+1}^m g_i a_{w_i}(t), \quad (B2)$$

where we have taken $t_- \to -\infty$, and also used the fact that

$$\Theta(t_{-} \leqslant t + \tau_{j} - \tau_{i} \leqslant t) = \begin{cases} 1/2 & \text{if } j = i \\ 1 & \text{if } j < i \\ 0 & \text{otherwise,} \end{cases}$$

and as a second step neglected delay $\tau_i \simeq \tau_i$. Using Eqs. (B1) and (B2), we have that

$$i\frac{da_{w_j}(t)}{dt} = \sum_{u} (\mathbf{H}_{\text{eff}})_{w_j,u} a_u(t) + g_j^* b_{t+\tau_j}(t_-) \quad \text{if } j \in \{1, 2, \dots, m\},$$

$$i\frac{da_v(t)}{dt} = \sum_{u} (\mathbf{H}_{\text{eff}})_{u,v} a_u(t) \quad \text{otherwise,}$$

where

$$(\mathbf{H}_{\mathrm{eff}})_{w_j,w_j} = J_{w_j,w_j} - i \frac{|g_j|^2}{2} \quad \text{for} \quad j \in \{1, 2, \cdots, m\},$$

$$(\mathbf{H}_{\mathrm{eff}})_{w_j,w_i} = J_{w_j,w_i} - i g_j^* g_i \quad \text{for} \quad j, i \in \{1, 2, \cdots, m\} \text{ and } j < i,$$

$$(\mathbf{H}_{\mathrm{eff}})_{u,v} = J_{u,v} \quad \text{otherwise}.$$

We can integrate this equation explicitly,

$$\begin{pmatrix} a_{1}(t) \\ a_{2}(t) \\ \vdots \\ a_{N}(t) \end{pmatrix} = e^{-i\mathbf{H}_{\text{eff}}(t-t_{-})} \begin{pmatrix} a_{1}(t_{-}) \\ a_{2}(t_{-}) \\ \vdots \\ a_{N}(t_{-}) \end{pmatrix} - i \sum_{n=1}^{m} \int_{t_{-}}^{t} e^{-i\mathbf{H}_{\text{eff}}(t-s)} g_{n}^{*} b_{s+\tau_{n}}(t_{-}) \mathbf{e}_{w_{n}} ds,$$
(B3)

where \mathbf{e}_{w_n} is a basis vector with a value of 1 at position w_n and 0 elsewhere. Now, we are interested in

$$S(\omega,\nu) = [b_{\omega}(t_{+}),b_{\nu}^{\dagger}(t_{-})] = \langle 0|b_{\omega}(t_{+})b_{\nu}^{\dagger}(t_{-})|0\rangle = \frac{1}{2\pi} \int_{-\infty}^{\infty} \int_{-\infty}^{\infty} e^{i\omega\tau} e^{-i\nu\sigma} \langle 0|b_{\tau}(t_{+})b_{\sigma}^{\dagger}(t_{-})|0\rangle d\tau d\sigma.$$

Note that as $t_+ \to \infty$ and $t_- \to -\infty$, as well as neglecting the time delay by assuming $\tau_1 \simeq \tau_2 \simeq \cdots \simeq \tau_m \simeq 0$, we can write

$$b_{\tau}(t_{+}) = b_{\tau}(t_{-}) - i \sum_{i=1}^{m} g_{i} a_{w_{i}}(\tau - \tau_{i}) \Theta(t_{-} \leqslant \tau - \tau_{i} \leqslant t_{+}) \simeq b_{\tau}(t_{-}) - i \sum_{i=1}^{m} g_{i} a_{w_{i}}(\tau) \Theta(t_{-} \leqslant \tau \leqslant t_{+}),$$

$$= b_{\tau}(t_{-}) - i \left[\mathbf{g}^{\mathsf{T}} e^{-i\mathbf{H}_{\mathrm{eff}}(\tau - t_{-})} a(t_{-}) - i \sum_{n=1}^{m} \int_{t_{-}}^{\tau} \mathbf{g}^{\mathsf{T}} e^{-i\mathbf{H}_{\mathrm{eff}}(\tau - s)} g_{n}^{*} b_{s + \tau_{n}}(t_{-}) \mathbf{e}_{w_{n}} ds \right],$$

where $\mathbf{g} = \sum_{n=1}^{m} g_n \mathbf{e}_{w_n}$. Therefore,

$$b_{\tau}(t_{+})b_{\sigma}^{\dagger}(t_{-}) = \delta(\tau - \sigma) - \sum_{n=1}^{m} \int_{t_{-}}^{\tau} \mathbf{g}^{\mathrm{T}} e^{-i\mathbf{H}_{\mathrm{eff}}(\tau - s)} g_{n}^{*} \mathbf{e}_{w_{n}} \delta(s + \tau_{n} - \sigma) ds$$

$$= \delta(\tau - \sigma) - \sum_{n=1}^{m} \mathbf{g}^{\mathrm{T}} e^{-i\mathbf{H}_{\mathrm{eff}}(\tau - \sigma + \tau_{n})} g_{n}^{*} \mathbf{e}_{w_{n}} \Theta(t_{-} \leqslant \sigma - \tau_{n} \leqslant \tau)$$

$$\simeq \delta(\tau - \sigma) - \mathbf{g}^{\mathrm{T}} e^{-i\mathbf{H}_{\mathrm{eff}}(\tau - \sigma)} \mathbf{g}^{*} \Theta(t_{-} \leqslant \sigma \leqslant \tau),$$

where we again assumed $\tau_n \simeq 0$. Inserting this into the scattering matrix, we obtain

$$\begin{split} S(\omega, \nu) &= \frac{1}{2\pi} \int_{-\infty}^{\infty} \int_{-\infty}^{\infty} \delta(\tau - \sigma) e^{i\omega\tau} e^{-i\nu\sigma} d\tau d\sigma - \frac{1}{2\pi} \int_{-\infty}^{\infty} \int_{-\infty}^{\tau} \mathbf{g}^{\mathrm{T}} e^{-i\mathbf{H}_{\mathrm{eff}}(\tau - \sigma)} \mathbf{g}^{*} e^{i\omega\tau} e^{-i\nu\sigma} d\tau d\sigma, \\ &= \delta(\omega - \nu) - \frac{1}{2\pi} \int_{0}^{\infty} \int_{-\infty}^{\infty} \mathbf{g}^{\mathrm{T}} e^{-i\mathbf{H}_{\mathrm{eff}} t} \mathbf{g}^{*} e^{i\omega t} e^{i(\omega - \nu)\sigma} dt d\sigma, \\ &= \delta(\omega - \nu) \bigg[1 - \int_{0}^{\infty} \mathbf{g}^{\mathrm{T}} e^{-i(\mathbf{H}_{\mathrm{eff}} - \omega I)t} \mathbf{g}^{*} dt \bigg], \\ &= \delta(\omega - \nu) [1 - i\mathbf{g}^{\mathrm{T}} (\mathbf{H}_{\mathrm{eff}} - \omega I)^{-1} \mathbf{g}^{*}]. \end{split}$$

This can be further expressed in terms of the eigenvectors and eigenvalues of the Hamiltonian to obtain

$$S(\omega, \nu) = \delta(\omega - \nu) \left[1 + i \sum_{i,j,\alpha} \frac{g_i g_j^* M_{\alpha, w_i, w_j}^{(1)}}{\omega - E_\alpha} \right].$$

2. State preparation for χ_{ν} measurement

The classical algorithm for obtaining the χ value was found to be unstable. In this section, we will demonstrate that if we have the capability to control the nonlinearity, enabling us to turn it on and off at will, there exists a protocol that overcomes this instability. Suppose we want to measure the nonlinearity at a desired site $v \in \mathcal{V}$. First, we prepare the following NOON state in a two-port waveguide setup:

$$|\Psi_{\rm I}\rangle = \frac{1}{2}(|G\rangle \otimes |P_{\rm out}\rangle_{\rm ref} + e^{i\alpha}|P_{\rm in}\rangle \otimes |G\rangle_{\rm ref}),$$
 (B4)

where $|G\rangle$ is the zero photon state and α is a phase that we will pick later. Note that the reference port is not coupled to the lattice. $|P_{\text{out}}\rangle$ ($|P_{\text{in}}\rangle$) is the P-photon Fock state resulting from initializing the system at $(a_v^\dagger)^P |G\rangle/\sqrt{P!}$ and evolving it forward (back) in time. In Appendix B 2 a, we show how to compute the wave packets ψ_{in} and ψ_{out} , corresponding to the Fock states $|P_{\text{in}}\rangle$ and $|P_{\text{out}}\rangle$. In Appendix B 2 b, we further provide a concrete scheme to generate NOON states in (B4), given the wave packets ψ_{in} and ψ_{out} , starting from a NOON state in two harmonic oscillators and letting them controllably decay into the output ports. The next step is to let the wave function in Eq. (B4) evolve. As expected, the resulting wave function can be written as

$$|\Psi_{P,v}\rangle = \frac{1}{2}(|G\rangle \otimes |P_{\text{out}}\rangle_{\text{ref}} + e^{i\alpha}|P_{v}\rangle \otimes |G\rangle_{\text{ref}}),$$

where $|P_v\rangle = (a_v^{\dagger})^P |G\rangle/\sqrt{P!}$. Now if we turn on the nonlinearity for time $T_{\rm on}$ and neglect the diffusion of photons to the other sites, $|P_v\rangle$ will simply acquire a phase,

$$|\Phi_{P,v}
angle = rac{1}{\sqrt{2}}igg(|G
angle\otimes|P
angle_{ ext{ref}} + e^{i(lpha- heta_{v,P})}rac{a_v^{\dagger P}}{\sqrt{P!}}\otimes|G
angle_{ ext{ref}}igg),$$

and

$$\theta_{P,v} = \left(\mu_v P + \frac{\chi_v P(P-1)}{2}\right) T_{\text{on}}.$$

Finally, if let the system to decay into the port, the output wave function is,

$$|\Psi_{\rm F}\rangle = \frac{1}{2}(|G\rangle \otimes |P_{\rm out}\rangle_{\rm ref} + e^{i(\alpha - \theta_{v,P})}|P_{\rm out}\rangle \otimes |G\rangle_{\rm ref}).$$

This state is then passed through a 50-50 beam splitter, followed by a parity measurement on one of the beam splitter's outputs. Assuming that the beam splitter is described by $\binom{1/\sqrt{2}}{1/\sqrt{2}} - \frac{1/\sqrt{2}}{-1/\sqrt{2}}$, this measurement yields an expected value of $\cos \theta_{v,P}$ and $\sin \theta_{v,P}$ for the choice of $\alpha = 0, \pi/2$.

a. Computing $|\psi_{in}\rangle$ to initialize the system at $|P_v\rangle$

Here, we begin by initializing the system with P photons at site $v \in \mathcal{V}$, represented as $|P_v\rangle$. We then evolve the system backward (forward) in time to obtain the input (output) wave packet (Fig. 12). The Hamiltonian governing the system and the port can be expressed as

$$H = H_s + \int_{-\infty}^{\infty} \omega b_{\omega}^{\dagger} b_{\omega} d\omega$$
$$+ \int_{-\infty}^{\infty} (A^{\dagger} b_{\omega} + A b_{\omega}^{\dagger}) \frac{d\omega}{\sqrt{2\pi}} \quad \text{and } A = \sum_{u} g_{u} a_{u}.$$

Here, b_{ω} is the annihilation operator for the port at frequency ω and a_u is the annihilation operator of the bosonic mode at site $u \in \mathcal{V}$. g_u represents the coupling rate of site u to the port, and it is only nonzero for sites that have a coupling connection to the port. The system's Hamiltonian, H_s , is given by

$$H_s = \sum_{u} \omega_u a_u^{\dagger} a_u + \sum_{u,u' \in \mathcal{E}} J_{u,u'} a_u^{\dagger} a_{u'}.$$

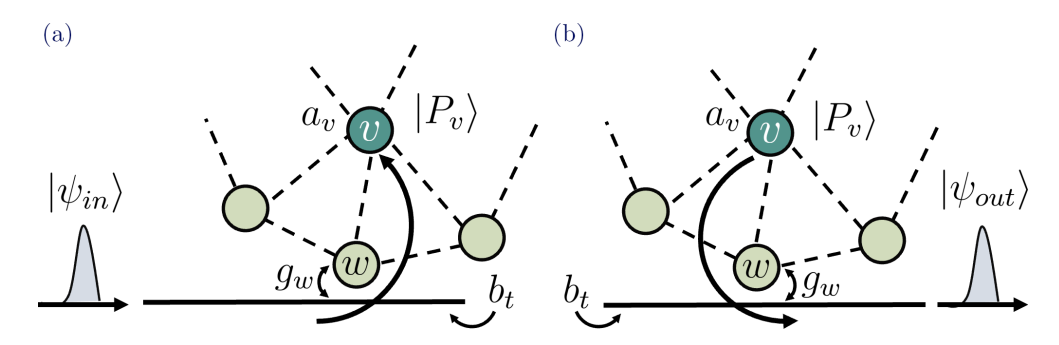


FIG. 12. (a) Initiating the lattice with a P-photon Fock state at site v and tracing its evolution backward in time to determine the input wave packet within the port. (b) Illustrating the output wave packet, representing the state of the port following the initialization of the lattice with $|P_v\rangle$ and its forward time evolution.

To analyze the system further, we work in the interaction picture with respect to the Hamiltonian of the port:

$$H_I = H_s + A^\dagger b_t + A b_t^\dagger \quad ext{and } b_t = rac{1}{\sqrt{2\pi}} \int_{-\infty}^{\infty} b_\omega e^{-i\omega t} d\omega.$$

The Hamiltonian for both the system and port preserves the excitation number, and there is no photon-photon interaction since the nonlinearity is switched off. Therefore, we analyze the single-particle problem with the initial state being $|\psi(0)\rangle = a_v^\dagger |0\rangle$ for $v \in \mathcal{V}$. The evolved wave function at time t can be represented as

$$|\psi(t)\rangle = \sum_{u} \alpha_{u}(t)a_{u}^{\dagger}|0\rangle + \int_{-\infty}^{\infty} F_{\tau}(t)b_{\tau}^{\dagger}|0\rangle d\tau,$$
 (B5)

with the initial condition values

$$\boldsymbol{\alpha}(0) = \mathbf{e}_v \quad \text{and } F_{\tau}(0) = 0.$$

Here, α is the vector of α_u , and \mathbf{e}_v is a basis vector with a value of 1 at position v and 0 elsewhere. Our objective is to find the input wave packet, which is described by $F_{\tau}(-\infty)$. We can derive the equations of motion for α and $F_{\tau}(t)$ as follows:

$$\frac{d\mathbf{\alpha}}{dt} = -i\mathbf{J}\mathbf{\alpha}(t) - i\mathbf{g}^*F_t(t), \tag{B6}$$

$$\frac{dF_{\tau}(t)}{dt} = -i\mathbf{g}^{\mathrm{T}}\boldsymbol{\alpha}(t)\delta(t-\tau). \tag{B7}$$

Here, **g** is a vector of g_u , and **J** is a matrix with elements $\mathbf{J}_{u,u'} = J_{u,u'}$. To simplify notation, we have assumed $\mathbf{J}_{u,u} = \omega_u$. Integrating the second equation, we obtain

$$F_{\tau}(t) = F_{\tau}(0) - i \int_{0}^{t} \mathbf{g}^{\mathsf{T}} \boldsymbol{\alpha}(t') \delta(t' - \tau) dt'$$
$$= 0 + \frac{i}{2} \mathbf{g}^{\mathsf{T}} \boldsymbol{\alpha}(\tau) \Theta(t \leqslant \tau \leqslant 0),$$

where

$$\Theta(t \leqslant \tau \leqslant 0) = \begin{cases} \frac{1}{2} & \text{if} \quad \tau \in \{t, 0\} \\ 1 & \text{if} \quad \tau \in (t, 0) \\ 0 & \text{otherwise.} \end{cases}$$

Therefore,

$$F_t(t) = \frac{i}{2} \mathbf{g}^{\mathrm{T}} \boldsymbol{\alpha}(t)$$

and

$$\frac{d\mathbf{\alpha}(t)}{dt} = -i\mathbf{J}\mathbf{\alpha}(t) + \frac{\mathbf{g}^*\mathbf{g}^{\mathrm{T}}}{2}\mathbf{\alpha}(t) = -i\mathbf{H}_{\mathrm{eff}}^{\dagger}\mathbf{\alpha}(t) \to \mathbf{\alpha}(t)$$
$$= e^{-i\mathbf{H}_{\mathrm{eff}}^{\dagger}t}\mathbf{e}_{\mathrm{u}}.$$

where

$$\mathbf{H}_{\text{eff}} = \mathbf{J} - i \frac{\mathbf{g}^* \mathbf{g}^{\text{T}}}{2}.$$

Thus.

$$F_{\tau}(t) = i(\mathbf{g}^{\mathrm{T}} e^{-i\mathbf{H}_{\mathrm{eff}}^{\dagger} \tau} \mathbf{e}_{v}) \Theta(t \leqslant \tau \leqslant 0).$$

This results in

$$F_{\tau}(-\infty) = i\mathbf{g}^{\mathrm{T}} e^{-i\mathbf{H}_{\mathrm{eff}}^{\dagger} \tau} \mathbf{e}_{v}.$$

Similarly, we can determine the wave packet for $t \to \infty$:

$$F_{\tau}(\infty) = -i\mathbf{g}^{\mathrm{T}}e^{-i\mathbf{H}_{\mathrm{eff}}\tau}\mathbf{e}_{v}.$$

It's important to note that the imaginary part of the eigenvalues of $\mathbf{H}_{\rm eff}$ are either zero or negative. Assuming there are no bound states in the system, there are no zero eigenvalues, indicating that $e^{-i\mathbf{H}_{\rm eff}^{\dagger}\tau}$ ($e^{-i\mathbf{H}_{\rm eff}\tau}$) approaches zero as $\tau \to -\infty$ ($\tau \to \infty$).

Finally, for the case with P photons, we can write the input and output wave function as

$$\begin{aligned} |\psi_{\rm in}\rangle &= \frac{1}{\sqrt{P!}} \bigg(\int_{-\infty}^{\infty} F_{\tau}(-\infty) b_{\tau}^{\dagger} d\tau \bigg)^{P} |0\rangle \quad \text{ and } |\psi_{\rm out}\rangle \\ &= \frac{1}{\sqrt{P!}} \bigg(\int_{-\infty}^{\infty} F_{\tau}(\infty) b_{\tau}^{\dagger} d\tau \bigg)^{P} |0\rangle. \end{aligned}$$

b. Relationship between g(t) and $|\psi_{in}\rangle$

Consider a cavity that is coupled to a port, with the coupling coefficient g(t) varying with time. Initially, the cavity is in an excited state and gradually emits a photon into the port. The objective is to determine the time-dependent parameter g(t) to obtain the desired final wave function $|\psi_{\rm in}\rangle$, expressed as

$$|\psi_{\mathrm{in}}
angle = \int_{-\infty}^{\infty} F_{\mathrm{\tau}}(\infty) b_{\mathrm{\tau}}^{\dagger} d \mathrm{\tau}.$$

In the interaction picture with respect to the port's Hamiltonian, the Hamiltonian can be represented as

$$H(t) = g(t)b_t^{\dagger}a + \text{H.c.}$$

Here, a is the annihilation operator for the cavity mode and b_t is the annihilation operator for the port mode at time t. Consequently, we can describe the combined wave function of the cavity and the port as follows:

$$|\psi(t)\rangle = \alpha(t)a^{\dagger}|0\rangle + \int_{-\infty}^{\infty} F_{\tau}(t)b_{\tau}^{\dagger}|0\rangle d\tau.$$

The initial conditions are set as

$$\alpha(0) = 1$$
 and $F_{\tau}(0) = 0$.

The equation of motion is then given by

$$\dot{\alpha}a^{\dagger}|0\rangle + \int_{-\infty}^{\infty} \dot{F}_{\tau}(t)b_{\tau}^{\dagger}|0\rangle d\tau = -iH|\psi(t)\rangle.$$

By applying $\langle 0|a$ and $\langle 0|b_{\tau}$ from the left, we obtain

$$\dot{\alpha}(t) = -ig^*(t)F_t(t)$$
 and $\dot{F}_{\tau}(t) = -ig(t)\alpha(t)\delta(t-\tau)$.

Solving these equations results in

$$F_{\tau}(t) = \begin{cases} 0 & t < \tau \\ -\frac{i}{2}g(\tau)\alpha(\tau) & t = \tau, \quad \text{ and } \alpha(t) = e^{-\frac{1}{2}\int_0^t |g(s)|^2 ds} \\ -ig(\tau)\alpha(\tau) & t > \tau. \end{cases}$$

As t approaches infinity, we can establish a relationship between $F_{\tau}(\infty)$ and g(t) as follows:

$$F_{\tau}(\infty) = -ig(\tau)e^{-\frac{1}{2}\int_0^{\tau}|g(s)|^2ds}.$$

Finally, it can be demonstrated that

$$g(\tau) = \frac{iF_{\tau}(\infty)}{\sqrt{1 - \int_0^{\tau} |F_s(\infty)|^2 ds}}.$$

3. Error analysis in χ_{ν} measurement

a. Error in $|P_v\rangle$ due to linear tomography accuracy

We can establish an upper bound on the error associated with initializing P photons at any lattice site, taking into account deviations from the true values of the linear coefficients in the Hamiltonian. Consider the precision ϵ_0 of the parameters $J_{u,v}$ and μ_u in the linear Hamiltonian $H^{(1)}$. We denote the measured linear Hamiltonian as $\hat{H}^{(1)}$. Suppose the input wave function is $|\psi_{\rm in}\rangle$, which is described by the $F_{\tau}(-\infty)$ values derived in Sec. B 2 a. We need to solve Eq. (B6) with the initial condition values:

$$\alpha(-\infty) = 0$$
 and $\hat{F}_{\tau}(-\infty) = i\mathbf{g}^{\mathrm{T}}e^{-i\hat{\mathbf{H}}_{\mathrm{eff}}^{\dagger}\tau}\mathbf{e}_{v}$.

Therefore,

$$F_t(t) = \hat{F}_t(-\infty) - i \int_{-\infty}^t \mathbf{g}^{\mathrm{T}} \boldsymbol{\alpha}(t') \delta(t'-t) dt'$$
$$= \hat{F}_t(-\infty) - \frac{i}{2} \mathbf{g}^{\mathrm{T}} \boldsymbol{\alpha}(t).$$

Inserting this into the derivative of $\alpha(t)$:

$$\begin{aligned} \frac{d\alpha}{dt} &= -i\mathbf{H}_{\text{eff}}\boldsymbol{\alpha} - i\mathbf{g}^*\hat{F}_t(-\infty) \\ &= -i\hat{\mathbf{H}}_{\text{eff}}\boldsymbol{\alpha} + i(\hat{\mathbf{H}}_{\text{eff}} - \mathbf{H}_{\text{eff}})\boldsymbol{\alpha} - i\mathbf{g}^*\hat{F}_t(-\infty), \end{aligned}$$

It should be noted that the true evolved wave function is obtained using the true Hamiltonian $\mathbf{H}_{\mathrm{eff}}$ instead of the reconstructed one. By solving the above equation,

$$\boldsymbol{\alpha}(t) = \int_{-\infty}^{t} e^{-i\hat{\mathbf{H}}_{\text{eff}}(t-s)} \mathbf{g}^* \hat{F}_s(-\infty) ds$$
$$-\int_{-\infty}^{t} e^{-i\hat{\mathbf{H}}_{\text{eff}}(t-s)} (\hat{\mathbf{H}}_{\text{eff}} - \mathbf{H}_{\text{eff}}) \boldsymbol{\alpha}(s) ds$$

at t = 0:

$$\boldsymbol{\alpha}(0) - \mathbf{e}_v = \int_{-\infty}^0 e^{i\hat{\mathbf{H}}_{\text{eff}}s} (\mathbf{H}_{\text{eff}} - \hat{\mathbf{H}}_{\text{eff}}) \boldsymbol{\alpha}(s) ds$$
$$= \int_0^\infty e^{-i\hat{\mathbf{H}}_{\text{eff}}s} (\mathbf{H}_{\text{eff}} - \hat{\mathbf{H}}_{\text{eff}}) \boldsymbol{\alpha}(-s) ds.$$

It can be noticed that $\hat{\mathbf{H}}\text{eff} - \mathbf{H}\text{eff}$ is a sparse matrix with a maximum of d nonzero elements in each row or column, where d is the degree of the graph describing the system's couplings. The value for each of these elements is also bounded by the linear tomography error ϵ_0 . Therefore:

$$\|\hat{\mathbf{H}}_{\text{eff}} - \mathbf{H}_{\text{eff}}\| \leqslant (d+1)\epsilon_0.$$

Here, we introduce the additional assumption,

$$||e^{-i\hat{\mathbf{H}}_{\text{eff}}s}|| \leqslant C_0\lambda_0 e^{-\lambda_0 s},$$

with coefficients C_0 and λ_0 , which can be a function of the total number of sites in the system N. This assumption implies that there are no bound states in the system, and any initial excitation in the system will decay exponentially to the port in time. Furthermore, C_0/λ_0 can be used as the propagation time T_{prop} for an excitation in the system to decay out of the lattice. Thus, considering $\|\alpha(s)\| \leq 1$:

$$\|\boldsymbol{\alpha}(0) - \mathbf{e}_v\| \leqslant \int_0^\infty \|e^{-i\hat{\mathbf{H}}_{\text{eff}}s}\| \|\hat{\mathbf{H}}_{\text{eff}} - \mathbf{H}_{\text{eff}}\| ds$$
$$\leqslant \frac{C_0}{\lambda_0} \epsilon_0(d+1).$$

Now we are interested in the distance between,

$$||P_v\rangle - |\hat{P}_v\rangle|| = \sqrt{2\text{Re}(1 - \langle \hat{P}_v|P_v\rangle)},$$

where

$$|\hat{P}_v\rangle = \frac{(a_v^{\dagger})^P}{\sqrt{P!}}|0\rangle,$$

$$|P_v\rangle = \frac{(\hat{a}_v^\dagger)^P}{\sqrt{P!}}|0\rangle = \frac{(\boldsymbol{\alpha}^{\mathrm{T}}(0)\mathbf{a}^\dagger + \int F_{\tau}(0)b_{\tau}^\dagger d\tau)^P}{\sqrt{P!}}|0\rangle.$$

The second equation is written from Eq. (B5). The inner product can be obtained as follows:

$$\langle P_v | \hat{P}_v \rangle = \frac{1}{P!} \langle 0 | (a_v)^P (\hat{a}_v^{\dagger})^P | 0 \rangle = [a_v, \hat{a}_v^{\dagger}]^P = (\mathbf{e}_v^{\mathsf{T}} \boldsymbol{\alpha}(0))^P,$$

Here we used Wick's theorem. Intuitively, we should choose P pairs between each a_v and \hat{a}_v , and there are P! ways to do that. We can write

$$\langle P_v | \hat{P}_v \rangle \geqslant 1 - P \| \boldsymbol{\alpha}(0) - \mathbf{e}_v \|.$$

Inserting this into the distance measure:

$$||P_v\rangle - |\hat{P}_v\rangle|| \leqslant \epsilon_1$$
 and $\epsilon_1 = \sqrt{\frac{2C_0}{\lambda_0}\epsilon_0(d+1)P}$. (B8)

This provides an upper bound on the error associated with initializing *P* photons at any lattice site.

b. Error in $|\phi_{P,v}\rangle$ due to photon diffusion to other sites

After preparing state $|P_v\rangle$, the nonlinearity is activated for a duration of $T_{\rm on}$. This time period should be sufficiently long to allow for the measurable accumulation of the phase induced by the nonlinearity. However, it should also be short enough to prevent the P photons from diffusing to neighboring sites. To quantify the latter condition, let H be the full Hamiltonian that includes on-site anharmonicities, linear on-site terms, and coupling terms. We can define H_χ as the same Hamiltonian H without the coupling terms, that is,

$$H - H_{\chi} = \sum_{v,u \in \mathcal{E}} J_{v,u} a_v^{\dagger} a_u.$$

The wave function at time $T_{\rm on}$ evolving with the Hamiltonian H_{χ} can be expressed as

$$|\phi_{P,v}
angle = e^{-iH_\chi T_{
m on}}|P_v
angle = e^{-i(\mu_v P + \chi_v rac{P(P-1)}{2})T_{
m on}}|P_v
angle.$$

Since there are no coupling terms in H_{χ} , all P photons remain at site u and the evolved wave function simply acquires a phase. When the system evolves under the full Hamiltonian H, the wave function at time $T_{\rm on}$ is

$$|\hat{\phi}_{P,v}\rangle = e^{-iHT_{\rm on}}|P_v\rangle.$$

We can quantify the distance between $|\hat{\phi}_{P,v}\rangle$ and $|\phi_{P,v}\rangle$ as

$$\||\hat{\phi}_{P,v}\rangle - |\phi_{P,v}\rangle\|^2 = 2\text{Re}(1 - \langle \hat{\phi}_{P,v} | \phi_{P,v} \rangle),$$

using the derivative of $\langle \hat{\phi}_{P,v} | \phi_{P,v} \rangle$ with respect to time:

$$\frac{d}{ds}\langle \hat{\phi}_{P,v} | \phi_{P,v} \rangle = \frac{d}{ds} \langle P_v | e^{iHs} e^{-iH_{\chi}s} | P_v \rangle$$
$$= i \langle \hat{\phi}_{P,v}(s) | H - H_{\chi} | \phi_{P,v}(s) \rangle.$$

Therefore:

$$\||\hat{\phi}_{P,v}\rangle - |\phi_{P,v}\rangle\|^2 \leqslant 2\int_0^{T_{\text{on}}} |\langle \hat{\phi}_{P,v}(s)|H - H_{\chi}|\phi_{P,v}(s)\rangle|ds.$$

We can express the term in the integral as

$$\begin{split} \||\hat{\phi}_{P,v}\rangle - |\phi_{P,v}\rangle\|^2 \\ \leqslant 2 \int_0^{T_{\text{on}}} \sum_{u,u'} |J_{u',u}| (|\langle \phi_{P,v}(s)| a_{u'}^{\dagger} a_u | \hat{\phi}_{P,v}(s) \rangle|) \, ds \\ = 2 \int_0^{T_{\text{on}}} \sum_{u',u} |J_{u',u}| (|\langle P| a_{u'}^{\dagger} a_u | \hat{\phi}_{P,v}(s) \rangle|) \, ds \end{split}$$

$$=2\int_{0}^{T_{\text{on}}}\sum_{u\in\mathcal{N}_{v}}|J_{v,u}|\sqrt{P}\left|\langle P-1|a_{u}|\hat{\phi}_{P,v}(s)\rangle\right|ds$$

$$\leqslant2\int_{0}^{T_{\text{on}}}\sum_{s}J\sqrt{P}\sqrt{\langle\hat{\phi}_{P,v}(s)|a_{u}^{\dagger}a_{u}|\hat{\phi}_{P,v}(s)\rangle}ds.$$

For the first equality, we use the fact that without the coupling terms in the Hamiltonian, the evolved wave function is just a phase applied on the state $|P_v\rangle$. $\langle P_v|a^{\dagger}_{u'}$ is zero unless u'=v, therefore, in the second equality, we just keep the terms that are neighbors of $v(u\in\mathcal{N}_v)$. For the last inequality, we use the Cauchy-Schwarz inequality, and we consider J to be the maximum value of $J_{u,v}$ over u,v:

$$\||\phi_{P,v}\rangle - |\hat{\phi}_{P,v}\rangle\|^2 \leqslant 2J\sqrt{P} \int_0^{T_{\text{on}}} \sum_{u \in \mathcal{N}_v} \sqrt{N_u(s)} \, ds.$$
 (B9)

The number operator at site u is defined as

$$\hat{N}_u = a_u^{\dagger} a_u$$
 and $N_u(s) = \langle \hat{\phi}_{P,v}(s) | a_u^{\dagger} a_u | \hat{\phi}_{P,v}(s) \rangle$

To find the upper bound on the number of photons at site u, we solve the differential equation for the operator \hat{N}_u in the Heisenberg picture:

$$\frac{d\hat{N}_u}{ds} = -i[\hat{N}_u, H] = i \sum_{v \in \mathcal{N}_u} (J_{u,v} a_u^{\dagger} a_v + J_{v,u} a_v^{\dagger} a_u).$$

Therefore, the upper bound for the derivative of number operator expectation is obtained as the following:

$$\frac{d}{ds} \langle \hat{\phi}_{P,v}(s) | \hat{N}_{u} | \hat{\phi}_{P,v}(s) \rangle$$

$$\leqslant \sum_{v \in \mathcal{N}_{u}} J(|\langle \hat{\phi}_{P,v}(s) | a_{u}^{\dagger} a_{v} | \hat{\phi}_{P,v}(s) \rangle|$$

$$+ |\langle \hat{\phi}_{P,v}(s) | a_{v}^{\dagger} a_{u} | \hat{\phi}_{P,v}(s) \rangle|),$$

$$\leqslant 2J \sum_{v \in \mathcal{N}_{u}} \sqrt{N_{u}(s) N_{v}(s)},$$

which implies

$$\frac{d}{ds}\sqrt{N_u(s)} \leqslant 2J \sum_{v \in \mathcal{N}_u} \sqrt{N_v(s)} \Rightarrow \sqrt{N_u(s)} \leqslant 2J d\sqrt{P}s,$$
(B10)

in which d is the maximum number of couplings at each site. Inserting Eq. (B10) into Eq. (B9):

$$\||\hat{\phi}_{P,v}\rangle - |\phi_{P,v}\rangle\| \leqslant \epsilon_2 \quad \text{and } \epsilon_2 = \sqrt{2P}JdT_{\text{on}}.$$
 (B11)

To ensure that the distance does not grow as a function of P, the evolution time should scale as $T_{\rm on} \propto 1/\sqrt{P}$. This choice ensures that, for short durations of $T_{\rm on}$, the diffusion of photons to other sites can be neglected.

c. Parity measurement error

Because of the error in the linear tomography of the Hamiltonian and the diffusion of the photons to the other neighbor sites, while the nonlinearity is on, the final wave function $|\hat{\Psi}_F\rangle$ will be different from the desired wave function $|\Psi_F\rangle$. The

distance between these two can be computed using Eqs. (B8) and (B11):

$$\||\hat{\Psi}_{F}\rangle - |\Psi_{F}\rangle\| \leqslant \epsilon_{3} \quad \text{and } \epsilon_{3} = 2\epsilon_{1} + \epsilon_{2}.$$
 (B12)

We define $\langle O \rangle_{\psi}$ to be the expectation value of the parity operator O on the state $|\Psi_F\rangle$, which results in the sine or cosine of the phase $\theta_{P,v}$ based on choosing the value of α . Now consider O_k to be the average outcome of k measurements of O on the state $|\hat{\Psi}_F\rangle$. With a probability of at least $1 - \delta$, we can derive the following using Chebyshev's inequality:

$$\operatorname{Prob}\left(|O_k - \langle O \rangle_{\hat{\psi}}| \leqslant \frac{1}{\sqrt{k\delta}}\right) \geqslant 1 - \delta, \tag{B13}$$

where $\langle O \rangle_{\hat{\psi}}$ is the expectation value of the parity operator O on state $|\hat{\Psi}_F\rangle$. Using the triangle inequality and defining

$$|O_k - \langle O \rangle_{\hat{\mathcal{U}}}| \geqslant |O_k - \langle O \rangle_{\psi}| - |\langle O \rangle_{\hat{\mathcal{U}}} - \langle O \rangle_{\psi}|.$$

By using the result in Eq. (B12) and $\|\hat{O}\| = 1$:

$$|\langle O \rangle_{\hat{\psi}} - \langle O \rangle_{\psi}| \leq 2||O|| |||\hat{\Psi}_{F}\rangle - |\Psi_{F}\rangle|| = 2\epsilon_{3}.$$

Inserting this into Eq. (B13):

$$\operatorname{Prob}(|O_k - \langle O \rangle_{\psi}| \leqslant \epsilon_4) \geqslant 1 - \delta \quad \text{and } \epsilon_4 = 2\epsilon_3 + \frac{1}{\sqrt{k\delta}}.$$
(B14)

Note that we interpret O_k as the sine or cosine of $(\mu_v P + \frac{P(P-1)}{2}\chi_{v,\text{est}})T_{\text{on}}$, with $\chi_{v,\text{est}}$ as the estimation of χ_v .

Calculating the error for the χ_v value solely using sine or cosine functions is not straightforward. This difficulty arises because the derivative of the inverse cosine or sine can become infinite for specific values of χ_v . To address this issue, we conduct 2k measurements and derive the following bounds based on Eq. (B14):

$$|\cos(\chi_1\theta) - \cos(\chi_2\theta)|$$

 $\leq \epsilon_4 \quad \text{and } |\sin(\chi_1\theta) - \sin(\chi_2\theta)| \leq \epsilon_4.$

Here, χ_1 represents the real value, and χ_2 is the estimated value. If ϵ_4 is small enough, then either $|\cos(\chi_2\theta)| \le 1 - \epsilon_4$ or $|\sin(\chi_2\theta)| \le 1 - \epsilon_4$. Consider the case where $|\sin(\chi_2\theta)| \le 1 - \epsilon_4$. We define $\varrho_i = \cos(\chi_i\theta)$. Note that for any $\rho \in [\rho_1, \rho_2]$,

$$|(1-\varrho^2)-(1-\varrho_2^2)| \le 2|\varrho-\varrho_2| \le 2\epsilon_4$$

from which it follows that

$$|(1-\varrho^2)| \ge |(1-\varrho_2^2)| - 2\epsilon_4 \ge (1-\epsilon_4)^2 - 2\epsilon_3$$

Therefore,

$$\theta|\chi_1-\chi_2|=\int_{\varrho_1}^{\varrho_2}\frac{d\varrho}{\sqrt{1-\varrho^2}}\leqslant \frac{\epsilon_4}{\sqrt{(1-\epsilon_4)^2-2\epsilon_4}},$$

Now, assuming ϵ_4 is small enough (in particular, $\epsilon_4 \leqslant \frac{1}{4}$), $\theta | \chi_1 - \chi_2 | \leqslant 4\epsilon_4$. A similar analysis can be performed if $|\cos(\chi_2 \theta)| \leqslant 1 - \epsilon_3$. Therefore, with a probability of least $1 - 2\delta$, $\chi_{v,\text{est}}$ satisfies

$$|\chi_{v,\mathrm{est}} - \chi_v| \leqslant \Delta \quad \text{where} \quad \Delta = \frac{8\epsilon_4}{P(P-1)T_{\mathrm{on}}} = \frac{8}{P(P-1)T_{\mathrm{on}}} \left[4\sqrt{2\frac{C_0}{\lambda_0}PN(d+1)\epsilon_0} + 2\sqrt{2P}JdT_{\mathrm{on}} + \frac{1}{\sqrt{\delta k}} \right].$$

Now for $P \gg 1$, we choose $T_{\text{on}} \leqslant O(1/\sqrt{P})$, $\epsilon_0 \leqslant O(1/P)$, $\delta, k = \Theta(1)$, and obtain that

$$P \simeq \left\lceil \frac{16}{\Delta} \left(\frac{2}{T_{\text{on}}} \sqrt{\frac{2C_0}{\lambda_0} (d+1)\epsilon_0} + \sqrt{2}Jd \right) \right\rceil^{2/3} \leqslant O(\Delta^{-2/3}).$$

- I. Carusotto, A. A. Houck, A. J. Kollár, P. Roushan, D. I. Schuster, and J. Simon, Photonic materials in circuit quantum electrodynamics, Nat. Phys. 16, 268 (2020).
- [2] M. J. Hartmann, Quantum simulation with interacting photons, J. Opt. 18, 104005 (2016).
- [3] B. M. Anderson, R. Ma, C. Owens, D. I. Schuster, and J. Simon, Engineering topological many-body materials in microwave cavity arrays, Phys. Rev. X 6, 041043 (2016).
- [4] J. C. Owens, M. G. Panetta, B. Saxberg, G. Roberts, S. Chakram, R. Ma, A. Vrajitoarea, J. Simon, and D. I. Schuster, Chiral cavity quantum electrodynamics, Nat. Phys. 18, 1048 (2022).
- [5] N. Schine, A. Ryou, A. Gromov, A. Sommer, and J. Simon, Synthetic Landau levels for photons, Nature (London) 534, 671 (2016).

- [6] M. Hafezi, S. Mittal, J. Fan, A. Migdall, and J. Taylor, Imaging topological edge states in silicon photonics, Nat. Photon. 7, 1001 (2013).
- [7] D. Hangleiter, I. Roth, J. Eisert, and P. Roushan, Precise Hamiltonian identification of a superconducting quantum processor, arXiv:2108.08319.
- [8] R. Ma, C. Owens, A. LaChapelle, D. I. Schuster, and J. Simon, Hamiltonian tomography of photonic lattices, Phys. Rev. A 95, 062120 (2017).
- [9] J. Haah, R. Kothari, and E. Tang, Learning quantum Hamiltonians from high-temperature Gibbs states and real-time evolutions, Nat. Phys. **20**, 1027 (2024).
- [10] A. Saxena, A. Manna, R. Trivedi, and A. Majumdar, Realizing tight-binding Hamiltonians using site-controlled coupled cavity arrays, arXiv:2210.05070.

- [11] S. Mittal, V. V. Orre, G. Zhu, M. A. Gorlach, A. Poddubny, and M. Hafezi, Photonic quadrupole topological phases, Nat. Photon. 13, 692 (2019).
- [12] E. Kim, X. Zhang, V. S. Ferreira, J. Banker, J. K. Iverson, A. Sipahigil, M. Bello, A. González-Tudela, M. Mirhosseini, and O. Painter, Quantum electrodynamics in a topological waveguide, Phys. Rev. X 11, 011015 (2021).
- [13] D. Burgarth, K. Maruyama, and F. Nori, Coupling strength estimation for spin chains despite restricted access, Phys. Rev. A 79, 020305(R) (2009).
- [14] C. Di Franco, M. Paternostro, and M. S. Kim, Hamiltonian tomography in an access-limited setting without state initialization, Phys. Rev. Lett. **102**, 187203 (2009).
- [15] D. Burgarth and K. Maruyama, Indirect Hamiltonian identification through a small gateway, New J. Phys. 11, 103019 (2009).
- [16] K. Maruyama, D. Burgarth, A. Ishizaki, T. Takui, and K. B. Whaley, Application of indirect Hamiltonian tomography to complex systems with short decoherence times, Quantum Info. Comput. 12, 763 (2012).
- [17] D. Burgarth, K. Maruyama, and F. Nori, Indirect quantum tomography of quadratic Hamiltonians, New J. Phys. 13, 013019 (2011).
- [18] H. L. Stormer, D. C. Tsui, and A. C. Gossard, The fractional quantum Hall effect, Rev. Mod. Phys. 71, S298 (1999).
- [19] M. Hafezi, E. A. Demler, M. D. Lukin, and J. M. Taylor, Robust optical delay lines with topological protection, Nat. Phys. 7, 907 (2011).
- [20] J. Zhang and M. Sarovar, Quantum Hamiltonian identification from measurement time traces, Phys. Rev. Lett. 113, 080401 (2014).
- [21] J. Zhang and M. Sarovar, Identification of open quantum systems from observable time traces, Phys. Rev. A 91, 052121 (2015)
- [22] A. Sone and P. Cappellaro, Hamiltonian identifiability assisted by a single-probe measurement, Phys. Rev. A 95, 022335 (2017)
- [23] Y. Wang, D. Dong, A. Sone, I. R. Petersen, H. Yonezawa, and P. Cappellaro, Quantum Hamiltonian identifiability via a similarity transformation approach and beyond, IEEE Trans. Autom. Control 65, 4632 (2020).
- [24] D. Burgarth and K. Yuasa, Quantum system identification, Phys. Rev. Lett. 108, 080502 (2012).
- [25] D. Burgarth and A. Ajoy, Evolution-free Hamiltonian parameter estimation through Zeeman markers, Phys. Rev. Lett. 119, 030402 (2017).
- [26] C. Kokail, R. van Bijnen, A. Elben, B. Vermersch, and P. Zoller, Entanglement Hamiltonian tomography in quantum simulation, Nat. Phys. 17, 936 (2021).
- [27] T. Ramos and J. J. García-Ripoll, Multiphoton scattering tomography with coherent states, Phys. Rev. Lett. 119, 153601 (2017).
- [28] I. A. Fedorov, A. K. Fedorov, Y. V. Kurochkin, and A. Lvovsky, Tomography of a multimode quantum black box, New J. Phys. 17, 043063 (2015).

- [29] V. Giovannetti, S. Lloyd, and L. Maccone, Quantum metrology, Phys. Rev. Lett. 96, 010401 (2006).
- [30] R. Ma, B. Saxberg, C. Owens, N. Leung, Y. Lu, J. Simon, and D. I. Schuster, A dissipatively stabilized Mott insulator of photons, Nature (London) **566**, 51 (2019).
- [31] L. Pezzè, A. Smerzi, M. K. Oberthaler, R. Schmied, and P. Treutlein, Quantum metrology with nonclassical states of atomic ensembles, Rev. Mod. Phys. 90, 035005 (2018).
- [32] J. J. Bollinger, W. M. Itano, D. J. Wineland, and D. J. Heinzen, Optimal frequency measurements with maximally correlated states, Phys. Rev. A 54, R4649 (1996).
- [33] M. J. Holland and K. Burnett, Interferometric detection of optical phase shifts at the Heisenberg limit, Phys. Rev. Lett. 71, 1355 (1993).
- [34] B. C. Sanders, Quantum dynamics of the nonlinear rotator and the effects of continual spin measurement, Phys. Rev. A 40, 2417 (1989).
- [35] S. Xu and S. Fan, Input-output formalism for few-photon transport: A systematic treatment beyond two photons, Phys. Rev. A 91, 043845 (2015).
- [36] R. Trivedi, K. Fischer, S. Xu, S. Fan, and J. Vuckovic, Fewphoton scattering and emission from low-dimensional quantum systems, Phys. Rev. B 98, 144112 (2018).
- [37] R. Trivedi, M. Radulaski, K. A. Fischer, S. Fan, and J. Vučković, Photon blockade in weakly driven cavity quantum electrodynamics systems with many emitters, Phys. Rev. Lett. 122, 243602 (2019).
- [38] S. Boixo, A. Datta, S. T. Flammia, A. Shaji, E. Bagan, and C. M. Caves, Quantum-limited metrology with product states, Phys. Rev. A 77, 012317 (2008).
- [39] S. Boixo, A. Datta, M. J. Davis, S. T. Flammia, A. Shaji, and C. M. Caves, Quantum metrology: Dynamics versus entanglement, Phys. Rev. Lett. 101, 040403 (2008).
- [40] D. Xie, C. Xu, and A. M. Wang, Quantum estimation of Kerr nonlinearity in driven-dissipative systems, Res. Phys. 42, 105957 (2022).
- [41] W. P. Su, J. R. Schrieffer, and A. J. Heeger, Solitons in polyacetylene, Phys. Rev. Lett. 42, 1698 (1979).
- [42] J. K. Asbóth, L. Oroszlány, and A. Pályi, A short course on topological insulators, Lect. Notes Phys. 919, 1 (2016).
- [43] X. Zhang, E. Kim, D. K. Mark, S. Choi, and O. Painter, A superconducting quantum simulator based on a photonic-bandgap metamaterial, Science 379, 278 (2023).
- [44] A. J. Kollár, M. Fitzpatrick, and A. A. Houck, Hyperbolic lattices in circuit quantum electrodynamics, Nature (London) **571**, 45 (2019).
- [45] M. R. Wall and D. Neuhauser, Extraction, through filter-diagonalization, of general quantum eigenvalues or classical normal mode frequencies from a small number of residues or a short-time segment of a signal. I. Theory and application to a quantum-dynamics model, J. Chem. Phys. 102, 8011 (1995).